



Politecnico di Torino

Master's Degree in Biomedical Engineering A.Y. 2024/2025

Determination of the effectiveness of polymeric nanoparticles loaded with mRNA encoding TIMP-3 released from a thermosensitive Poloxamer hydrogel matrix for melanoma treatment

Supervisors:

Prof. VALENTINA ALICE CAUDA

Prof. CRISTINA FORNAGUERA

Candidate:

ELISA BATTUELLO

Contents

Αk	ost	ract	3
1.11	ntro	oduction	4
	1.1	Melanoma	4
	E	pidemiology and risk factors	4
	9	Staging and clinical management	5
	1.2	Nanotechnology- mediated drug delivery systems in melanoma treatment	7
	F	Polymeric nanosystems	7
	F	Poly-(β- amino ester)s based nanovehicles	8
	(Dligopeptide modified Poly-(β- amino ester)s	9
	F	Poly (β-amino esters) in melanoma treatment	10
	1.3	Hydrogels as reservoirs for sustained delivery of nanotherapeutics	10
	H	-lydrogels	11
	F	Poloxamers- based hydrogels	12
	1.4	Proteolytic remodelling in melanoma	14
	T	The metzincin proteases in metastatic melanoma	14
	T	Fissue Inhibitor of Metalloproteinases 3	16
2.	(Objectives	19
3.	Mc	aterials	20
	3.1	Reagents	20
	3.2	Cell lines	21
4.	Me	ethods	22
	4.1	Formulations	22
	r	mRNA loaded nanoparticles	22
	F	P407/P188 Hydrogel	22
	4.2	Characterization of the system	24
	F	Rheological analysis	24
	5	Scanning Electron Microscopy	25
	4.3	In vitro cell viability studies	25
	N	MTT assay	25

Evaluation of the biological effect of T3-NPs	26
Hydrogel biocompatibility assay	26
4.4 In vitro efficacy analysis	27
Sample preparation	27
Western Blot for TIMP3 relative quantification	28
ELISA for MMP-9 evaluation	28
5. Results	29
5.1 Rheological analysis	29
Rheological characterization of the P407/P188 hydrogel formulation	29
Loading Strategy: Effect of Final 10% (v/v) Water Addition on Gelation and Reproducibility	35
5.3 Scanning Electron Microscopy Characterization	39
5.4 In vitro cell viability studies	43
MTT assay	43
KH NPs cytotoxicity	45
Efficacy of the proposed treatment	46
Hydrogel Biocompatibility Assay	49
5.5 In vitro efficacy analysis	51
ELISA	51
Western Blot	52
5.6 Further characterisation	54
5.7 Conclusion	55
Ribliography	56

Abstract

Melanoma, an aggressive neoplasm with a propensity for metastasis, remains challenging to treat because of its rapid progression, high heterogeneity, and resistance to conventional chemotherapeutic agents. In this context, tissue inhibitor of metalloproteinases-3 (TIMP-3) has been shown to exert multifaceted anti-tumor activities through the induction of apoptosis, inhibition of matrix metalloproteinases (MMPs), suppression of angiogenesis, and a marked reduction in melanoma invasiveness, thereby representing a promising molecular target for therapeutic intervention. Previous studies have demonstrated that adenoviral-mediated delivery of TIMP-3 can effectively inhibit tumor formation and growth in vivo through mechanisms that include stabilization of death receptors, thereby sensitizing melanoma cells to apoptotic signals and impairing angiogenesis. Considering the drawbacks of viral vectors, this study employed polymeric nanoparticles (NPs) engineered to encapsulate mRNA encoding TIMP-3, based on cationic poly (beta-amino esters) (PBAEs). Although PBAE NPs have been widely investigated for gene and drug delivery, their integration into a thermosensitive hydrogel matrix has not been reported. The rationale for this combinational approach lies in the complementary functions of the two systems: while the nanoparticles offer robust protection and intracellular delivery of the mRNA encoding TIMP-3, the Poloxamer hydrogel serves as a depot that provides sustained, controlled release at the target site, reduces the frequency of administration, and minimizes systemic exposure and off-target effects. This work offers novel insight into the therapeutic potential of TIMP-3, with significant implications for advancing personalized cancer treatment.

1.Introduction

1.1 Melanoma

Skin cancer is among the most common malignancies worldwide and is broadly classified into two major categories: non-melanoma skin cancers (NMSC) and melanoma. Despite being less common than NMSC, melanoma accounts for nearly 73 % of skin-cancer-related deaths [1]. It is a malignant neoplasm arising from mutation in melanocytes, the pigment-producing cells primarily located in the basal epidermal layer. Once melanoma breaches the basement membrane and invades the dermis, it becomes more aggressive: tumor cells can enter lymphatic vessels, migrate to draining lymph nodes, and—if they evade immune surveillance—metastasize to other body sites.

Melanoma manifests as a pigmented lesion that undergoes dynamic changes over time in terms of asymmetry, border irregularity, colour variability, and increased diameter—a clinical description commonly summarized by the ABCDE criteria (Figure 1). Although the cutaneous form of melanoma is the most common, the disease can also manifests in non-cutaneous locations including mucosal surfaces, the uveal tract of the eye, and, less commonly, in extracutaneous sites due to aberrant melanocyte migration.

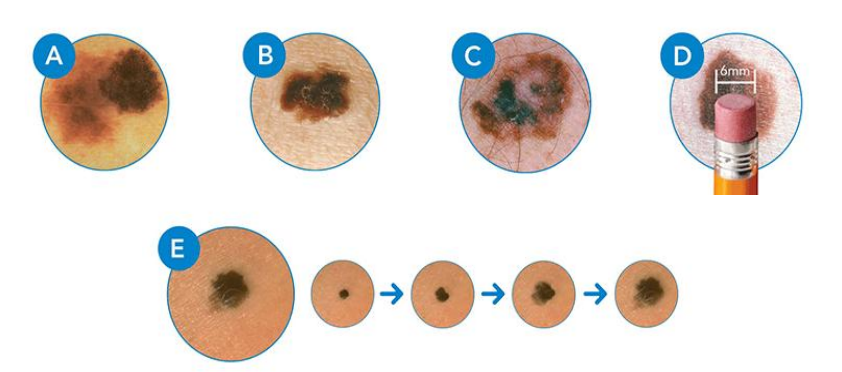


Figure 1: ABCDE clinical warning signs of cutaneous melanoma

Epidemiology and risk factors

In 2020, there were approximately 325,000 new cases of cutaneous melanoma globally, representing 1.7% of all cancer diagnoses, with around 57,000 deaths attributed to the disease. Epidemiological findings show that melanoma incidence and mortality patterns vary by age, sex, and geographic region, with countries such as Australia, New Zealand, North America, and parts of Europe reporting the highest disease burden [1]. Figure 2 shows the global age-standardised incidence distribution. Melanoma is a multifactorial disease that arises from an interplay between environmental exposures, genetic predisposition, phenotypic characteristics, and behavioural factors. The primary environmental determinant is exposure to ultraviolet radiation (UVR), which induces DNA damage through different mechanisms, with UVB causing direct DNA damage and UVA

contributing indirectly via the production of reactive oxygen species [2]. Phenotypic traits also play a significant role in increasing melanoma risk. Individuals with fair skin, light-coloured eyes, red or blonde hair, and a propensity to freckle or burn are markedly more susceptible, primarily due to lower levels of protective eumelanin and the relative abundance of the more photolabile pheomelanin [3]. Furthermore, a high density of melanocytic nevi, especially atypical or dysplastic nevi, has been associated with an elevated risk of melanoma [4]. Genetic factors, including family history and specific gene mutations-commonly in genes such as BRAF, NRAS, or CDKN2A—as well as immunosuppression are also key contributors to this malignancy [5].

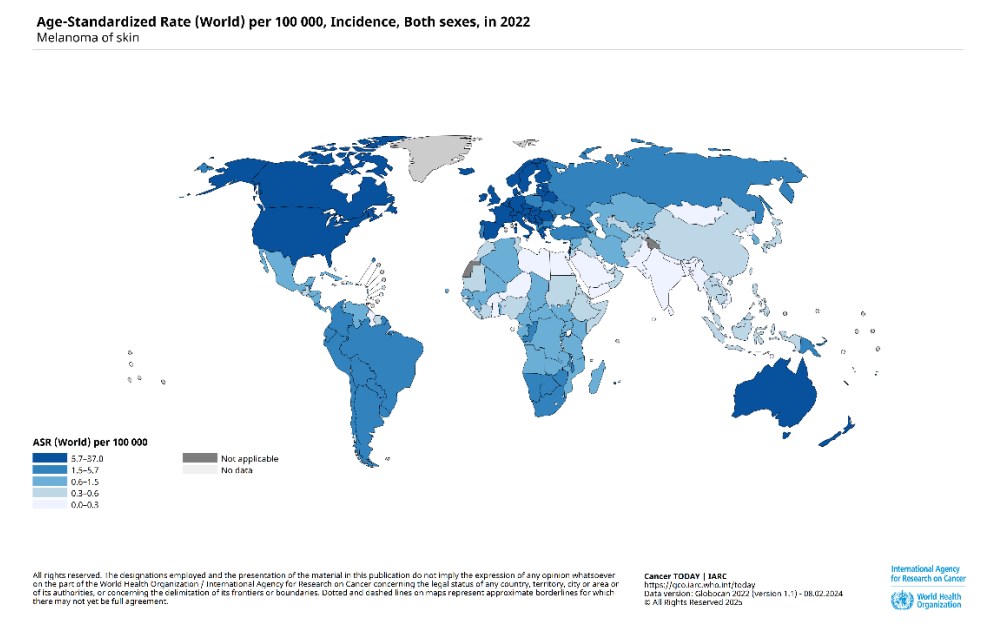


Figure 1: Global age-standardized incidence rates of cutaneous melanoma (https://gco.iarc.fr/today/en/dataviz/maps-heatmap?mode=population&cancers=16)

Staging and clinical management

Accurate staging of melanoma is crucial for prognostication and guiding treatment decisions. The American Joint Committee on Cancer (AJCC) melanoma staging system is widely adopted and utilizes the TNM classification scheme, which considers primary tumor characteristics (T), regional lymph node involvement (N), and distant metastases (M)[6], [7].

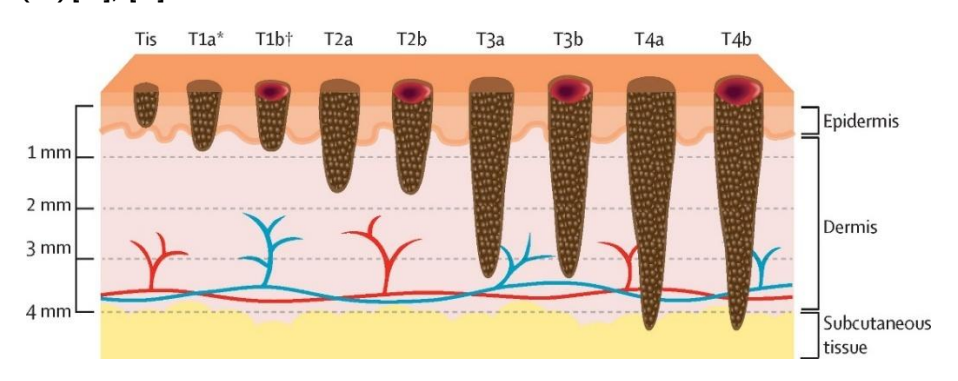


Figure 3: Cutaneous melanoma T categories [8]

Melanoma is classified into stages 0 to IV, with stage 0 limited to the epidermis, stages I and II defined by tumor thickness and ulceration, stage III involving lymphatic tissues, and stage IV indicating spread to vital organs.

The management of melanoma is highly stage dependent. Early-stage melanoma (up to stage II) can often be successfully treated with surgical resection, which remains the first-line option whenever feasible. Metastatic melanoma, which includes both stage III with unresectable regional disease and stage IV with distant metastases, represents one of the most challenging clinical scenarios in oncology and is managed primarily with systemic therapy (Figure 4). Chemotherapy with dacarbazine was the first approved systemic treatment for advanced melanoma, but its low response rates (5-12%) and minimal survival benefit have relegated its use to palliative or selected combination settings[9]. The introduction of BRAF and MEK inhibitors has significantly improved outcomes in patients with BRAF-mutated tumors; however, the development of resistance within 6-8 months remains a major clinical challenge [8]. Immunotherapy, particularly checkpoint inhibitors targeting CTLA-4 (ipilimumab) and PD-1 (nivolumab, pembrolizumab), has produced durable responses and significantly extended overall survival [8]. Combination immunotherapy further improves efficacy but increases toxicity, requiring careful patient selection[10]. High-dose interleukin-2 (IL-2) remains an option for selected cases, while intralesional administration offers localized control with fewer adverse effects [11]. Local approaches complement systemic treatments in selected patients. Surgical resection (metastasectomy) may achieve prolonged survival in oligometastatic disease. Radiotherapy, including stereotactic radiosurgery, is widely used for palliation and brain metastases. Novel strategies aim to overcome resistance and broaden therapeutic efficacy. These include adoptive T-cell therapy with tumorinfiltrating lymphocytes (TILs), cancer vaccines targeting melanoma-associated antigens, and new immune checkpoint inhibitors (e.g., LAG-3, TIGIT) currently under clinical investigation[11],[9].

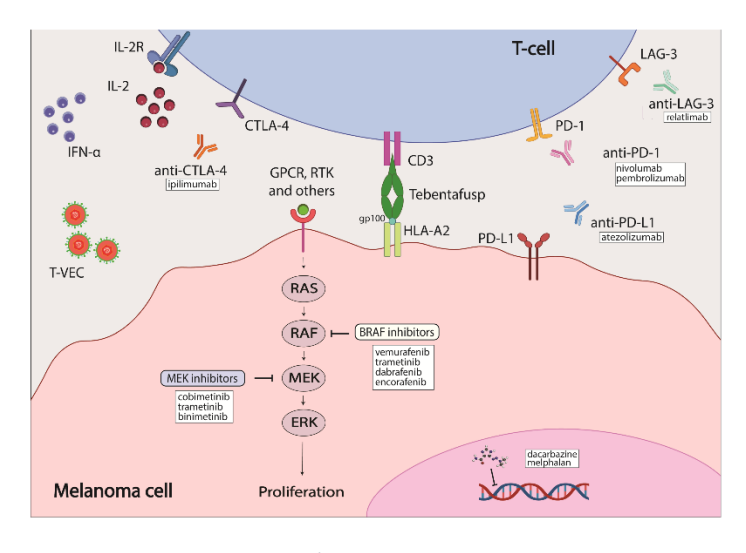


Figure 4: Melanoma therapies currently approved by the FDA [11]

1.2 Nanotechnology- mediated drug delivery systems in melanoma treatment

In recent years, nanotechnology-enhanced drug delivery systems have emerged as a promising approach to overcome the challenges associated with conventional therapies. Nanomedicines are defined as entities possessing at least one dimension at the nanoscale, developed for medical purposes such as diagnosis and treatment. Various nanocarriers – including liposomes, dendrimers, polymeric nanoparticles, metallic nanoparticles, and hybrid systems– have been developed to optimize systemic drug delivery in metastatic melanoma, each offering distinct advantages regarding biocompatibility, drug loading capacity, and targeting specificity [12], [13]. Depending on their intended application, nanocarriers can encapsulate different types of cargo, such as drugs, proteins, or genetic material. Optimal performance stems from rational design in which size and polydispersity govern cellular uptake, circulation time, and biodistribution [14], [15], [16]; surface chemistry and charge control stability, stealth, and targeting [17], [18]; and carrier–cargo interactions regulate loading and release kinetics[19]. Mechanical cues—including stiffness, strength, and adhesive behavior—also influence biodistribution and targeting efficiency.

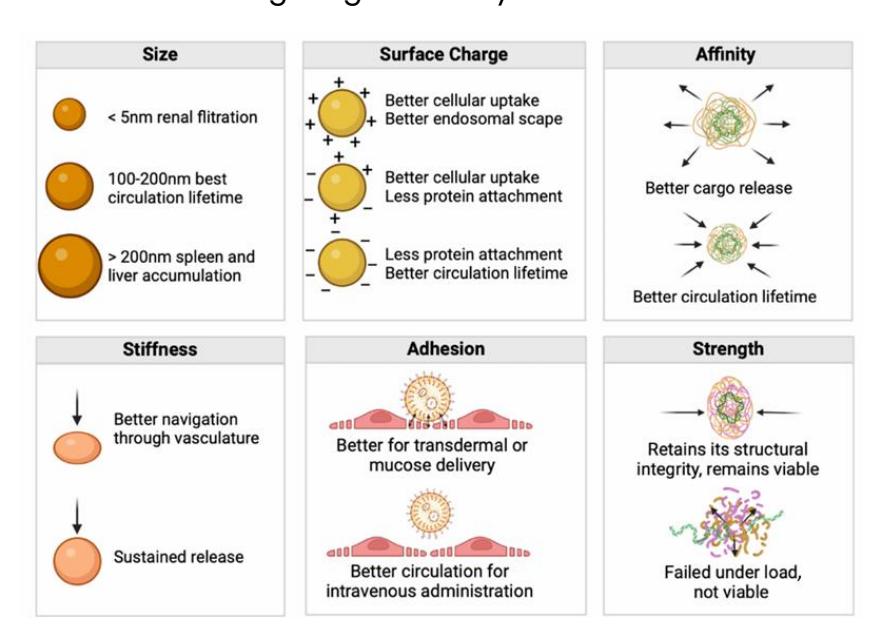


Figure 5: **Effect of different physicochemical and mechanical properties in drug delivery systems**

Polymeric nanosystems

Polymer-based nanomaterials are strong candidates for drug and gene delivery owing to their straightforward synthesis and functionalization, structural versatility, scalability, high transfection efficiency, low immunogenicity, and good biocompatibility. They can be derived from natural polymers (e.g., proteins or polysaccharides) or from synthetic polymers such as poly (lactic-co-glycolic acid) (PLGA) and poly (β -amino ester) s

(PBAEs). Polymer-based nanocarriers can be engineered as polymersomes, dendrimers, and polyplexes. Polymersomes are artificial vesicles formed from amphiphilic block copolymers and are attractive for co-encapsulating hydrophilic and hydrophobic cargos[20]. Dendrimers are highly branched, monodisperse macromolecules built stepwise; they can load compounds within internal cavities or via conjugation to surface functional groups[21]. Polyplexes are electrostatic complexes between cationic polymers and nucleic acids; the positive charge condenses the cargo and promotes cellular uptake across the negatively charged plasma membrane. Accordingly, cationic polymers such as poly(L-lysine) (PLL), polyethyleneimine (PEI), and poly(amidoamine) (PAMAM) dendrimers have been widely applied for gene delivery[22], [23], [24]. Despite their broad use and high transfection efficiency, some polycations can display significant cytotoxicity—e.g., PEI due to non-degradable backbones at physiological pH, and PLL owing to high charge density and limited biodegradability[25], [26]. To address this limitation, degradable polycations can be employed.

Poly-(β- amino ester)s based nanovehicles

Poly-(β -amino) esters (P β AEs) are a group of biodegradable cationic polymers first employed as nucleic acid carriers in 2000 by Lynn and colleagues[27]. Since then, growing interest in their application for immune and tumor gene modulation has driven their development into multifunctional delivery vehicles, leading to the preclinical demonstration of their immunotherapeutic efficacy nearly two decades after their initial description [28]. P β AEs are generally synthesized by Michael Addition reaction between diacrylates and primary amines or secondary diamines, or by ring- opening polymerization. These strategies are relatively simple, rapid, cost-effective and industrially scalable. In addition, they allow structural tuning of the polymer backbone according to the desired properties which, together with the broad spectrum of available monomers, confers high chemical versatility to these polymers.

PβAEs' structure (*Figure 6*) offers several advantages with respect to other carriers, thanks to their pH dependent charge, which promotes binding to negatively charged nucleic acids at slightly acidic pH, biocompatibility, biodegradability and high transfection efficiency. PßAEs building blocks contain hexyl monomers (C6), characterized by repeating ester groups that are biodegradable through hydrolysis and enzymatic cleavage by esterases. The resulting degradation products exhibit negligible toxicity to mammalian cells under physiological conditions [27]. Moreover, C6 monomers confer a degree of hydrophobicity to the polymers, allowing PβAEs nanoparticles to undergo freeze-drying and subsequent redispersion without compromising their functionality, a remarkable feature that enables long-term storage and improves the logistics of distribution [29]. The large number of protonable amino groups in the polymers makes them easily positively charged, allowing electrostatic binding to nucleic

acids, leading to quick-assembly and easy formation of polyplexes. This allows the formation of nanoparticles with minimal energy input, achieving entrapment efficiency and loading capacities with values above 70%[30]. These characteristics makes PβAEs ideal candidates for the delivery of a wide variety of nucleic acid types.

Figure 6: Chemical structure of the end-terminated acrylate pBAE polymer general backbone (n = 6-8 repeating units); R is the amine-derived side chain where functional groups and targeting moieties can be added.

Oligopeptide modified Poly-(β- amino ester)s

As mentioned previously, PßAEs can be synthetized by varying their structural components (e.g., backbone, side chains, and terminal groups), allowing for tailored properties. Within the GEMAT group, libraries of amine-rich oligopeptide end-modified PßAEs (OM-PßAEs) were designed as synthetic-biologic hybrid structures to enhance hydrophilicity and cationic charge, thereby improving genetic material encapsulation and transfection efficiency[31]. In this platform, the choice of terminal oligopeptide confers distinct functions: arginine (R)- and lysine(K)-modified variants maintain strong positive charge at physiological pH, promoting tight condensation of genetic cargo and efficient cellular uptake; histidine (H)-modified variants provide a proton-sponge effect that facilitates endosomal escape; and aspartic-acid (D)-modified variants temper surface charge to reduce nonspecific interactions and improve colloidal stability[32]. Because the peptides are cysteine-terminated, redox-sensitive crosslinking or site-selective conjugation is also possible.

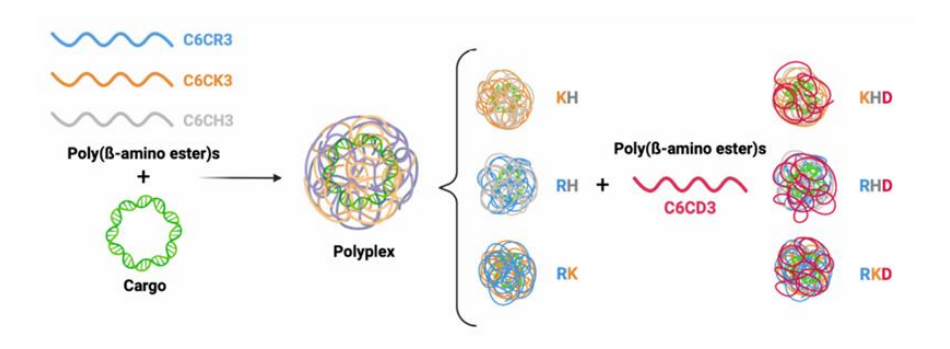


Figure 7: OM-pBAE polyplexes library

It has also been shown by the GEMAT group that formulating mixtures of OM-PBAEs is an effective approach to enhance gene delivery [33], and that tailoring the hydrophilicity-

hydrophobicity ratio of these polymers can significantly improve particle stability, loading capacity, and transfection efficiency [34].

Poly (β -amino esters) in melanoma treatment

In the context of melanoma treatment, pBAE nanoparticles have been employed for nucleic acid-based antitumor immunotherapies. Although viral vectors, such as oncolytic viruses and adenoviral platforms, are predominantly used for gene delivery in melanoma treatment, they present several limitations, such as low encapsulation capacity, safety concerns, and non-specific immune activation, which often leads to the elimination of the foreign material and prevents repeated administrations[35]. Together with high production costs and manufacturing difficulties, these challenges have driven the development of non-viral vectors as a safer and more feasible alternative. Among the nanomaterials explored, pBAE nanoparticles are particularly attractive due to their highly tunable physicochemical properties, broad cargo compatibility (plasmid DNA, mRNA, protein), efficient endosomal escape, and inherent biodegradability. Furthermore, the modularity of pBAE systems enables the co-delivery of mRNA with immune adjuvants, thereby generating a synergistic effect that enhances the overall immunogenicity and therapeutic efficacy.

In several murine melanoma models, treatment with pBAE-mediated gene delivery systems has been associated with notable reductions in tumor burden and improved survival rates, particularly when such systems are combined with immune checkpoint inhibitors or costimulatory ligands [36], [37]. Chu et al. used branched poly (β -amino ester)s to deliver a Bax-encoding plasmid into melanoma cells, achieving high transfection efficiency and inducing apoptosis with minimal cytotoxicity[38]. Mahin et al. used pBAE nanoparticles to deliver stimulator of interferon genes (STING) agonists, enhancing type I interferon responses and recruiting natural killer (NK) cells to the tumor site[39]. Moreover, pBAE-based mRNA vaccines have shown preclinical efficacy in models of metastatic melanoma by delivering antigen-encoding mRNA and adjuvants directly to splenic dendritic cells, resulting in significant antigenspecific T cell responses and tumor regression [40].

1.3 Hydrogels as reservoirs for sustained delivery of nanotherapeutics

Beyond their application as systemic nanocarriers, therapeutic nanoparticles have been increasingly combined with hydrogels to form systems for controlled drug delivery. Incorporating nanoparticles into the hydrogel matrix creates a dual-barrier system:

nanoparticles must first be released from the gel network and then internalized by cells via endocytosis.

Hydrogels

Hydrogels are soft materials composed of three-dimensional, cross-linked networks of hydrophilic polymers that can absorb and retain large amounts of water while maintaining structural integrity. They can be classified by source, polymer composition, network architecture, cross-linking mechanism, net charge, and responsiveness to environmental stimuli, as summarized in Figure 8. Network formation (gelation) arises from physical cross-links (e.g., hydrogen bonding, hydrophobic or ionic interactions), which are reversible and stimuli-responsive, or from chemical cross-links (covalent/photo-crosslinking), which confer higher mechanical stability and durability[41].

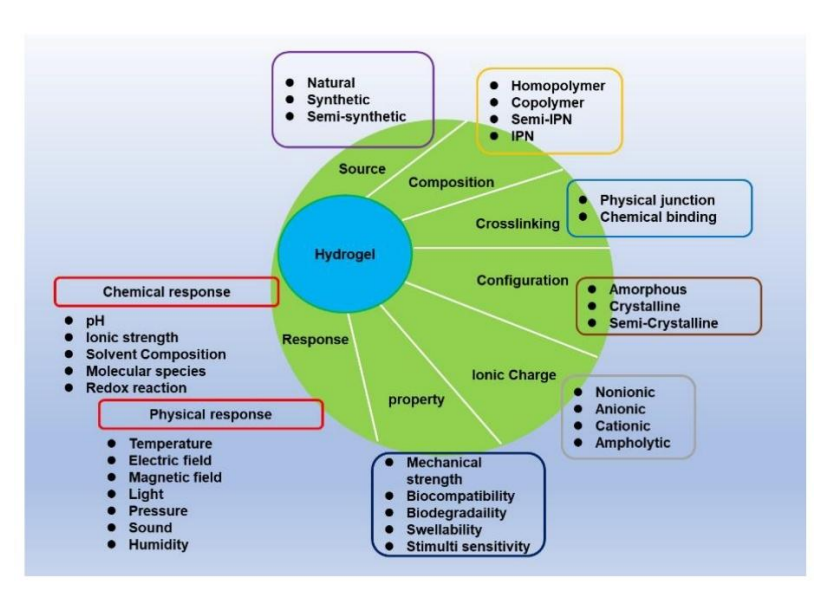


Figure 8: Classification of hydrogels [42]

Combining a tissue-like microenvironment with biocompatibility and tunable physicochemical properties, hydrogels have been widely used in a diverse range of biomedical fields, such as 3D cell cultures, drug delivery, wound dressing, and tissue engineering [42], [43], [44]. Mechanical behavior, degradation, and drug-release kinetics depend primarily on polymer composition and cross-linking; therefore, selection of the appropriate building blocks for the intended application is essential.

Among the various classes of hydrogels, stimuli-responsive systems are recognized for their potential in drug delivery[45]. Thermoresponsive hydrogels have attracted considerable attention due to their ability to transition from a sol to a gel state upon temperature changes. These materials typically incorporate polymers with a critical solution temperature (CST), such as the lower critical solution temperature (LCST) or upper critical solution temperature (UCST), which dictate their phase behavior under

thermal stimuli[46], [47]. The response arises from temperature-driven changes in polymer-solvent interactions, leading to phase separation driven by hydrophobic association and related molecular forces. Polymers exhibiting LCST behavior are particularly relevant for injectable applications, as they can be tuned to be water-soluble and low in viscosity at room temperature, facilitating handling and injection, and transition to gel near body temperature, allowing for in situ gelation. Among the most studied thermoresponsive systems there are poloxamers, poly(N-isopropylacrylamide) (PNIPAAm) and methylcellulose-based hydrogels [48].

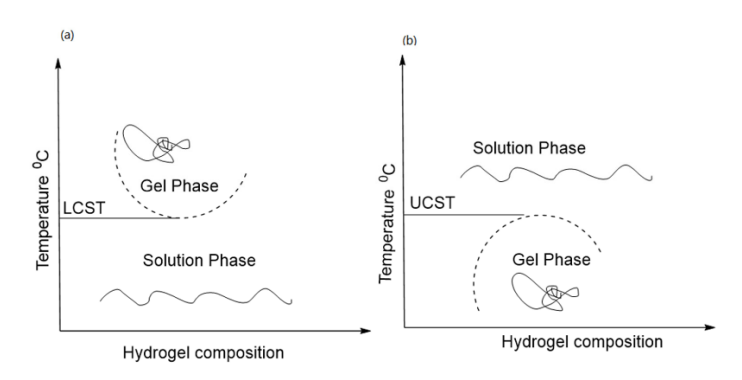


Figure 9: Thermoresponsive phase behavior of hydrogels. a) LCST-type; (b) UCST-type[47].

Poloxamers-based hydrogels

Poloxamers, also known as Pluronics®, are a class of synthetic, non-ionic ABA triblock copolymers composed of a central hydrophobic block of poly (propylene oxide) (PPO) flanked by two hydrophilic blocks of poly (ethylene oxide) (PEO) (Figure 10).

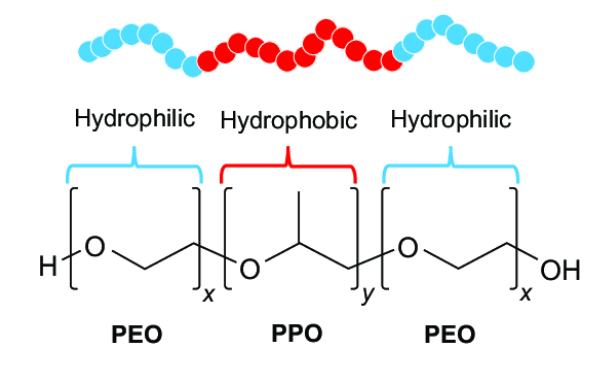


Figure 10: Chemical structure of Poloxamers

Owing to their amphiphilicity, they exhibit LCST behavior: in aqueous solutions, individual unimers are stabilized by hydrogen bonding at low temperature, whereas at the critical micelle concentration (CMC) and critical micellization temperature (CMT) the partial dehydration and reduced solubility of PPO drive self-assembly into micelles with PPO cores and PEO coronas [49], [50]. As micelle concentration increases, they approach a critical packing density, and micelle-micelle interactions lead to the establishment of a three-dimensional network that constitutes the gel phase. Higher concentrations not only lower the gelation temperature due to more facile micellization but also lead to a

more robust elastic network upon gelation, with the specific transition point being a function of the inherent properties of the polymer, the solvent, and the presence of eventual additives[51].

Several Pluronic copolymers with different physicochemical properties have been synthesized and are commercially available. The molecular weight of the poloxamer and the ratio of PEO to PPO determine its hydrophilic-lipophilic balance (HLB), which in turn affects solubility, self-assembly behavior, gelation properties, and ultimately the mechanical strength and erosion rate of the resulting hydrogels. Poloxamer 407 (P407), is widely used for its biocompatibility, low toxicity, and ease of regulatory acceptance because it is already included in several FDA-approved formulations. However, when used as a monocomponent formulation, P407 suffers from rapid gel erosion, insufficient mechanical strength, and a pronounced burst release of encapsulated payloads that ultimately limit its sustained release capacity. Additional challenges-especially for systemic use-include dose-dependent toxicity and potential effects on lipid metabolism. A common state-of-the-art approach to overcome these limitations is physical blending with other polymers or additives[52], [53]. Among these strategies, binary hydrogels composed of P407 and Poloxamer 188 (P188) have been employed in ocular, nasal and transdermal drug delivery[54], [55], [56] and are currently being evaluated in a clinical trial for the administration of 5-fluorouracil (5-FU) in colorectal cancer treatment ([57], Clinical Trial Search: NCT06385418). Owing to its lower molecular weight and higher PEO to PPO ratio, P188 tends to elevate the gelation temperature in P407 systems and can reduce gel erosion rate by enhancing gel strength. Moreover, its higher aqueous solubility its advantageous for formulations requiring lower viscosity and enhanced solubilization properties.



Figure 11: Chemical structure of Poloxamer 407 (left) and Poloxamer 188 (right)

Additionally, Poloxamers have a biological function of reversing multidrug resistance (MDR) by inhibiting p-glycoprotein efflux pumps, which expel drugs from target cells, thus potentially increasing drug efficacy.

Poloxamer-based nanocomposite hydrogels are commonly fabricated by the "cold method", in which the poloxamer is dissolved in cold aqueous media and the preformed polymeric nanoparticles are subsequently dispersed under vigorous mixing to ensure homogeneous distribution before warming to induce gelation. By coupling the thermoresponsive gelation of poloxamers with the controlled-release and targeting

features of polymeric nanoparticles, these composites address limitations observed when hydrogels or nanoparticles are used alone.

1.4 Proteolytic remodelling in melanoma

Melanoma's aggressive behaviour and rapid acquisition of therapy resistance create major clinical challenges. Resistant clones emerge through both genetic alterations and adaptive, non-genetic responses—phenotype switching, rewiring of signalling networks, and microenvironmental cues—that together sustain proliferation, promote invasion, and enable dissemination[58], [59].

The metzincin proteases in metastatic melanoma

superfamily of zinc-dependent The metzincin proteases, including matrix metalloproteinases (MMPs), A Disintegrin and Metalloproteinases (ADAMs), and ADAMs with Thrombospondin Motifs (ADAMTSs) plays a pivotal role in numerous biological processes, ranging from embryonic tissue remodelling and wound healing to the modulation of cell signaling pathways and the regulation of immune responses. Under physiological conditions, the activity of these proteases is tightly regulated by their endogenous inhibitors, the tissue inhibitors of metalloproteinases (TIMPs). In pathological settings, this homeostatic balance is disrupted, leading to enhanced invasion, migration, and the creation of a supportive tumor microenvironment [60]. In metastatic melanoma numerous members of these enzyme families are upregulated, while tissue inhibitor of metalloproteinase-3 (TIMP-3) is concurrently downregulated [61] [62]. Importantly, the proteolytic landscape is shaped not only by the elevated expression of individual MMPs and ADAMs, but also by their functional interplay, which creates a regulatory network where even subtle changes in the expression or activity of one family can amplify overall proteolysis and ultimately tip the balance toward an invasive and metastatic tumor phenotype.

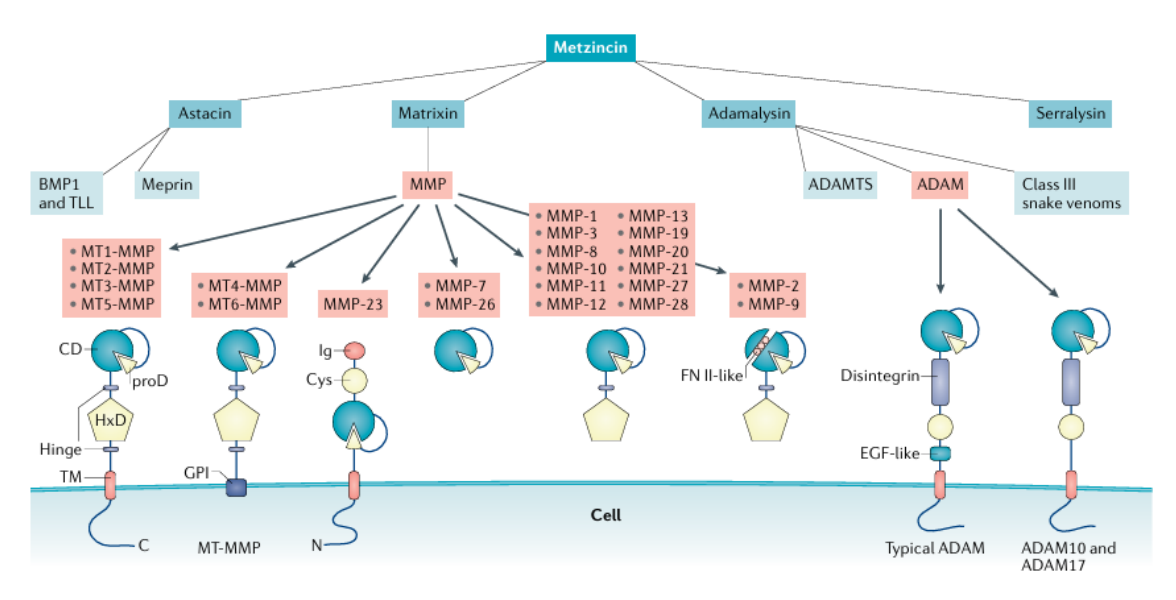


Figure 12: **Metzincin superfamily**. Phylogeny (top) and representative domain architectures (bottom) of the main subfamilies

MMPs are secreted or membrane-associated zinc-dependent endopeptidases that regulate ECM turnover under physiological conditions. In cancer, their overexpression promotes tumor progression by degrading ECM components, thereby facilitating invasion, and by releasing ECM-bound growth factors that sustain proliferative signaling [63]. In the most aggressive forms of malignant melanoma, MMP-2 and MMP-9 are markedly overexpressed and activated [64]. MMP-2, primarily produced by fibroblasts and stromal cells, promotes tumor progression by degrading adhesion molecules (e.g., E-cadherin, integrins) and modulating VEGF expression by activating integrin $\alpha V\beta 5$ through an autocrine mechanism [65], [66]. MMP-9 is responsible for the degradation of basement membrane components[67] and the activation of key growth factors (TGF- β , VEGF, TNF- α), which enhance proliferation, angiogenesis, and metastatic potential[68].

ADAM proteases mediate ectodomain shedding, a process that cleaves membrane-bound precursors to generate bioactive soluble factors. By disrupting cell–cell adhesion, this mechanism facilitates tumor cell detachment and invasion [69]. It also liberates growth factors and cytokines from the cell surface, activating autocrine and paracrine signaling pathways that drive proliferation and angiogenesis [70] [71]. In addition, ADAM activity can convert inactive membrane-associated precursors into active soluble mediators, further enhancing invasive behavior and modulating the immune response within the tumor microenvironment [72]. ADAM9, ADAM10, and ADAM17 are markedly overexpressed in metastatic melanoma. ADAM9 modulates interaction between melanoma cells and the surrounding ECM, ADAM10 has been implicated in the proteolytic shedding of key adhesion molecules, such as L1–CAM and VE–cadherin, and ADAM17, similarly, plays a pivotal role in shedding interleukin–6 receptors and other membrane-bound cytokines.

The ADAMTS family comprises enzymes that are critically involved in extracellular proteoglycan degradation, thereby influencing the composition and integrity of the ECM. Among its members, ADAMTS18 and ADAMTS4 have emerged as key players in metastatic melanoma. Genetic alterations in ADAMTS18 are associated with enhanced cell transformation, migration, and metastatic dissemination, primarily through reduced adhesion to laminin-I and increased motility, whereas the wild-type protein exerts tumor-suppressive effects by reinforcing cell-matrix adhesion and limiting invasion [73] [74]. ADAMTS4 exerts context-dependent effects in melanoma: the full-length, catalytically active enzyme promotes ECM cleavage, invasion, and VEGF-driven angiogenesis, whereas truncated or catalytically inactive forms can display antiangiogenic, tumor-suppressive activity [75], [76], [77].

The interdependent proteolytic network in metastatic melanoma provides a strong rationale for therapeutic strategies aimed at restoring proteolytic homeostasis.

Tissue Inhibitor of Metalloproteinases 3

TIMP-3 is a multifunctional regulator of extracellular proteolysis and the only TIMP with broad inhibitory activity against both matrix metalloproteinases and ADAM proteases. Notably, among the proteases discussed above, TIMP-3 inhibits MMP-2, MMP-9, ADAM10, ADAM17, and ADAMTS4. Unlike other TIMPs that are soluble, TIMP-3 is distinguished by its propensity to bind strongly to ECM components through electrostatic interactions with sulphated glycosaminoglycans [78], thereby remaining localized at sites of proteolysis and exerting prolonged inhibitory effects.

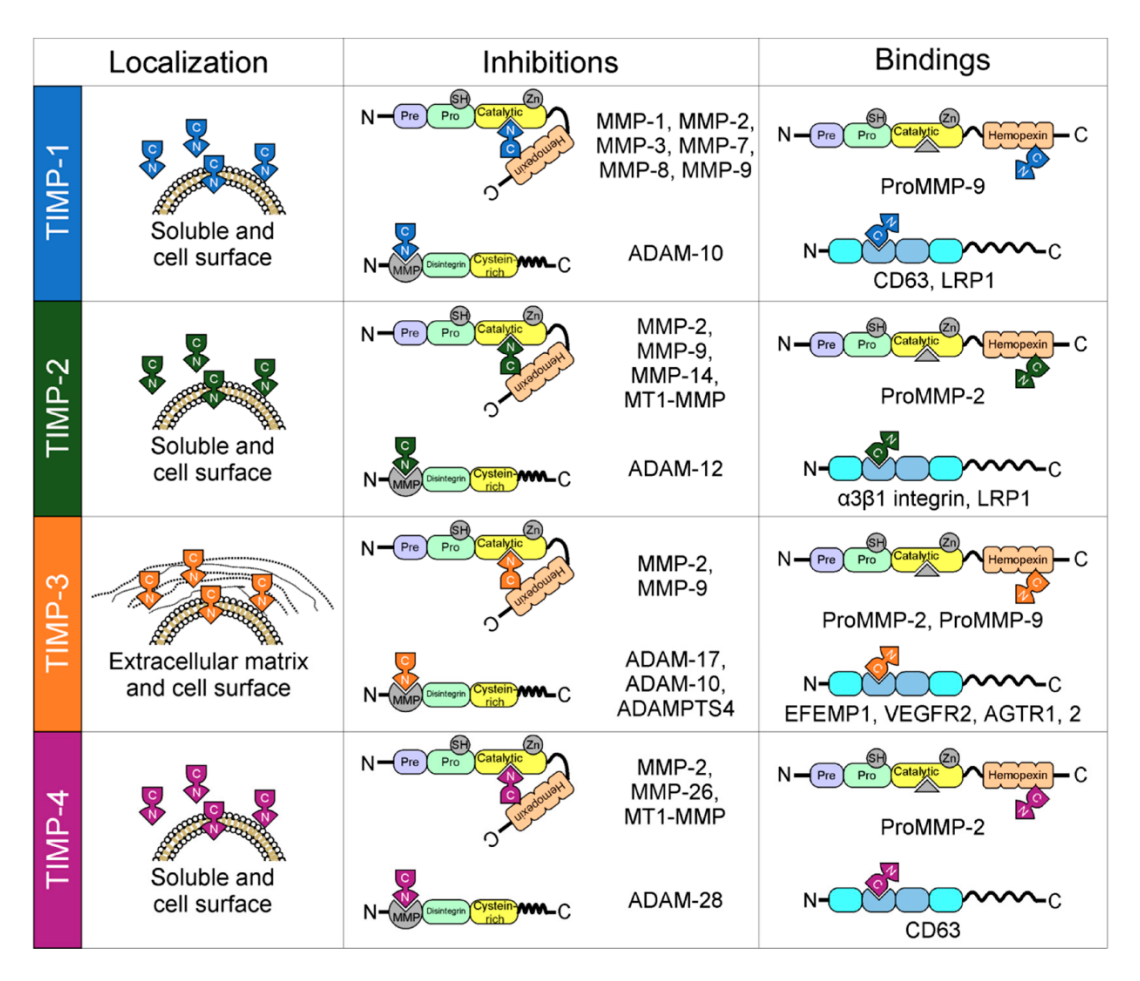


Figure 13: **Overview of the TIMP family**. Schematic comparison of TIMP-1/-2/-3/-4 showing (left) predominant localization, (middle) spectrum of metzincin inhibition, and (right) key binding partners beyond catalytic inhibition[63].

Human TIMP-3 is a 218-amino-acid protein with a two-domain architecture, each stabilized by three disulfide bonds formed by six cysteine residues. The mouse ortholog (221 aa) is highly conserved, retaining the same cysteine disulfide framework and C-terminal N-glycosylation site. The N-terminal domain mediates direct metalloproteinase inhibition, whereas the C-terminal domain supports additional binding interactions, including those with ECM components [79]. Across multiple studies expressing human TIMP-3 in mammalian systems, the protein appears as both unglycosylated (~24 kDa) and glycosylated (~27 kDa) isoforms; the latter predominates in biological settings and exhibits greater stability and ECM binding[80], [81]. Beyond protease inhibition, TIMP-3 forms non-inhibitory complexes with pro-MMP-2 and pro-MMP-9, and exerts antiangiogenic activity by blocking VEGF signaling through direct binding to VEGFR2 and by interacting with the angiotensin II type-2 receptor [82], [83].

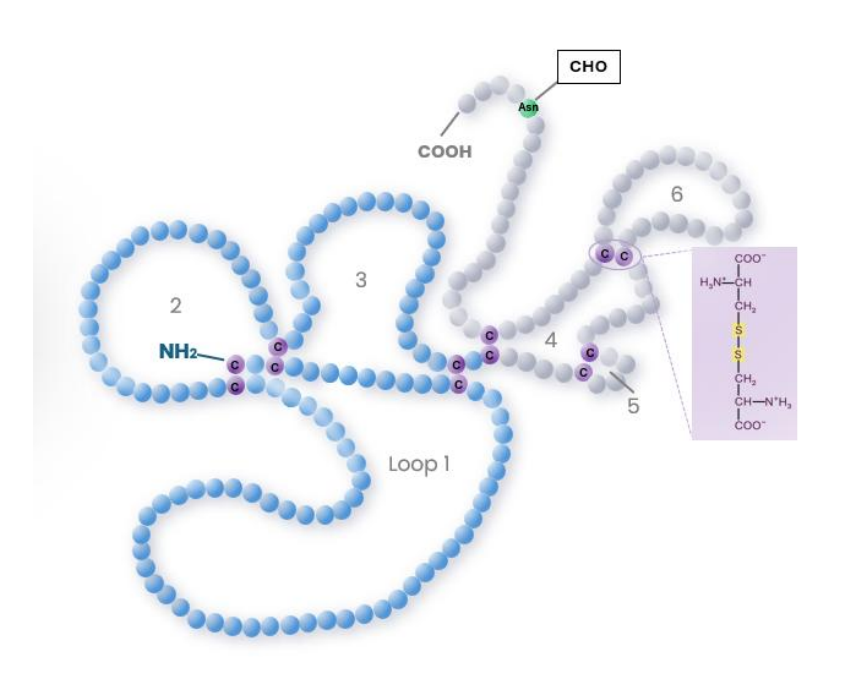


Figure 14: Schematic of human TIMP-3 primary/tertiary features.

Given its tumor-suppressive functions—mediated by multi-level inhibition of proteolytic and angiogenic pathways—restoring TIMP-3 expression in melanoma emerges as a promising therapeutic strategy. Between the late 1990s and early 2000s, a series of studies investigated adenovirus-mediated delivery of TIMP-3 in a broad range of cancer cell lines [84], [85], [86] [87]. In melanoma, beyond suppressing metalloproteinase activity and angiogenesis, TIMP-3 overexpression induces apoptosis both in vitro and in vivo[88] via the extrinsic death-receptor pathway, characterized by stabilization of TNF-R1, FAS, and TRAIL-R1, activation of caspase-8, and downstream caspase-3 cleavage[89]. Notably, in comparative experiments where other TIMP family members were also tested, TIMP-3 was the only inhibitor that consistently triggered apoptosis, reinforcing its uniqueness in its family. These findings suggests that TIMP-3 is a critical mediator of cell signaling pathways that govern cell survival and death.

2. Objectives

The main objective of this master's thesis was to characterize and assess the therapeutic potential of a previously designed nanoparticle-loaded hydrogel system, conceived as a novel local treatment for metastatic melanoma and proposed as an alternative to systemic administration.

In the preceding study, four formulations of TIMP-3 mRNA-loaded nanoparticles (T3-NPs) were incorporated into a hydrogel, and their release profiles were evaluated. The formulation containing lysine- and histidine-modified poly (β -amino esters) (KH NPs) emerged as the best candidate for further investigation.

As a continuation of the previous study, the present work main objective entails the following secondary objectives:

I. Hydrogel formulation characterization

- a. Rheological assessment of injectability and in situ gelation behavior
- b. Development of a protocol for SEM characterization to enable morphological analysis while minimizing dehydration-induced artifacts
- c. Assessment of a nanoparticle incorporation strategy using a mixing method compatible with nanoparticle stability

In vitro evaluation of treatment efficacy and safety

- a. Assessment of the biocompatibility of the hydrogel
- b. Evaluation of the cytotoxicity of KH T3-NPs
- c. Investigation of the anti-tumor efficacy of KH-T3 NPs and evaluation of potential effect on non-tumorigenic melanocytes lines, including comparison with a control formulation lacking therapeutic activity

II. Assessment of therapeutic molecular effects

- a. Confirmation of TIMP-3 upregulation in treated cells
- b. Assessment of MMP inhibition in vitro

3. Materials

3.1 Reagents

Sucrose, Sodium Acetate (AcONa), 4-(2-hydroxyethyl)-1-piperazineethanesulfonic acid (HEPES), Phosphate Buffered Saline (PBS), Thiazolyl Blue Tetra-zolium Bromide (MTT), Dimethyl Sulfoxide (DMSO) and Poloxamer 188 (Lutrol® F68) were purchased from Sigma-Aldrich. Poloxamer 407 (Kolliphor® P407) was obtained from BASF. Dulbecco's Modified Eagle Medium (DMEM), Roswell Park Memorial Institute 1640 Medium (RPMI), L-glutamine, penicillin and streptomycin were supplied by Biowest. Fetal Bovine Serum (FBS), culture plates and HTS Transwell plates were acquired from Corning, while individual Transwell insert for 24-well plate were obtained from Greiner. 12-o-tetradecanoyl phorbol-13-acetate (PMA) was purchased from TermoFisher.

The mRNA of Tissue Inhibitor of Metalloproteinases 3 (TIMP3) (PureBoost™ Modified TIMP3 mRNA) and the mRNA of GFP (PureBoost™ EGFP mRNA) were both obtained from Cellerna Bioscience. Rabbit poly-clonal TIMP-3 primary antibody was from Abcam (ab39184). Mouse monoclonal anti-β-Actin primary antibody (clone 2F1-1) was obtained from Biolegend. The Goat anti-Mouse secondary antibody was purchased from Biolegend (405306), while the Goat anti-Rabbit was from Novus Biologicals (NB7160). The chemiluminescent substrate for horseradish peroxidase (HRP), Immobilon® Western HRP Substrate (WBKLS), was acquired from Millipore.

Lysine- and histidine-end-modified poly(β -amino ester) (pBAE) polymers (referred to as K and H, respectively), which were used in this project, were synthesized by the Group of Materials Engineering (GEMAT) at the Institut Químic de Sarrià (Barcelona, Spain), following a two-step procedure, as previously described [90]. In brief, first, an acrylate-terminated polymer, C6 polymer, was synthesized by addition reaction of primary amines with diacrylates (at 1:1.2 M ratio of amine:diacrylate), resulting in the structure shown in *Figure 15A*. Subsequently, the resulting acrylate-terminated polymer was end-modified with either lysine or histidine to obtain the final pBAE structures, illustrated in *Figure 15B*.

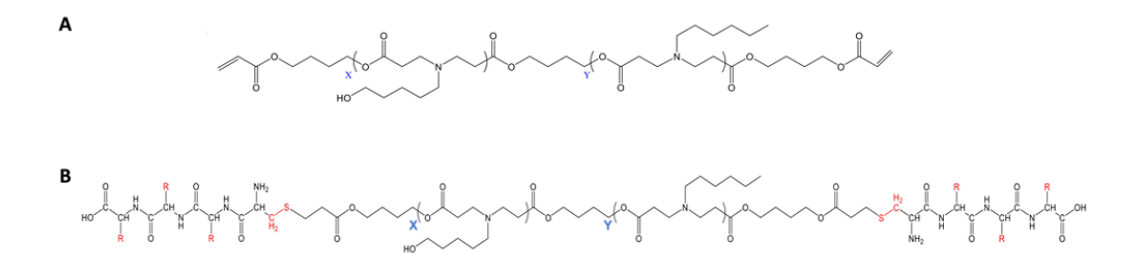


Figure 15: **Chemical structure of pBAE polymers**. A) Structure of the base C6 pBAE polymer, consisting of repeated ester groups formed by the reaction between hydrophilic amines and hydrophobic diacrylates, with a typical degree of polymerization of X+Y=5-7. B) Structure of OM-pBAEs, where oligopeptides are conjugated to the end-terminals of the C6 backbone.

3.2 Cell lines

Three different murine cell lines were employed in this study: two melanoma-derived lines -B16-F1 and B16-F10- and one non-tumorigenic melanocyte line, melan-a. B16-F1 subline was obtained from the parental B16 melanoma through a single round of in vivo selection and is characterized by relatively low metastatic potential. In contrast, B16-F10 was established after ten successive rounds of in vivo selection using Fidler's method, resulting in a markedly increased metastatic capacity, particularly to the lungs. Melan-A line was derived from melanocytes of embryonic C57BL/6 mouse skin, the same inbred strain from which the B16 melanoma originated. Melan-A cells retain the main features of normal melanocytes while being non-tumorigenic, thus providing a syngeneic and genetically comparable control for in vitro and in vivo studies alongside B16 sublines.

B16-F10 were purchased from ATCC (CRL-6475TM), while B16-F1 and melan-a were kindly provided by the Microenvironment and Metastasis Laboratory at the Centro Nacional de Investigaciones Oncológicas (PI: Hector Peinado; Madrid, Spain).

B16-F10 and B16-F1 cells were maintained in DMEM supplemented with 10% (v/v) FBS, 2 mM glutamine and 1% (v/v) penicillin-streptomycin.

Melan-a were cultured in RPMI medium, supplemented with 10% (v/v) FBS, 2 mM glutamine, 1% (v/v) penicillin/streptomycin and PMA at a concentration of 120 ng/mL.

All cells were cultured at 37° C, under 5% CO₂ /95% air atmosphere, to reach 70%-90% confluence. Afterwards, the maintenance cell passages were done in a 75 cm² flask.

4. Methods

4.1 Formulations

This study employed two pre-optimized formulations: OM-PBAEs nanoparticles encapsulating TIMP-3 mRNA developed by the GEMAT Group at Institut Químic de Sarrià, and a thermosensitive hydrogel composed of P407 and P188 designed by the MiNt group at University of Angers (PI: Prof. Guillaume Bastiat).

mRNA loaded nanoparticles

Based on previous experiments, KH was chosen as the formulation offering the best compromise between release kinetics from the P407/P188 hydrogel and transfection efficiency, as the presence of histidine allow proton sponge effect and proper delivery of the genetic material in the cytoplasm [91].

Two KH nanoparticle formulations were employed in this study: T3-NPs, encapsulating TIMP-3 mRNA, and GFP-NPs, loaded with enhanced green fluorescent protein (eGFP) mRNA as a negative control.

Nanoparticles were prepared at an N/P molar ratio -defined as the molar ratio between polymer amine groups (N) and nucleic acid phosphate groups (P)- of 75:1, which was previously shown to enable TIMP-3 mRNA loading into polymeric OM-PBAE nanoparticles with hydrodynamic diameters below 250 nm, low polydispersity index (PDI < 0.2), and high encapsulation efficiency (>80%)[92].

Equal volumes of nucleic acid solution (0.5 mg/mL of either TIMP3 mRNA or eGFP mRNA) and OM- PβAE polymer solution (12.5 mg/mL) were mixed in 12.5mM sodium acetate buffer (pH 5.2). The polymer formulation consisted of a mixture of lysine- and histidine-end-modified pBAE polymers (K and H, respectively) in a 60:40 weight ratio. The nucleic acid was added to the polymer solution, and mixed by pipetting, followed by 30 min of incubation at room temperature. After incubation, nanoprecipitation into an equal volume of RNAse-free water was performed to complete nanoparticle formation. Subsequently, the same volume of HEPES buffer (20 mM, pH 7.4) containing 4 wt% sucrose was added as cryo- and lyoprotectant. The final formulation was thus diluted 1:3 relative to the original incubation mixture.

P407/P188 Hydrogel

The injectable system investigated in this thesis consists of 90% thermosensitive hydrogel, acting as a carrier, and 10% KH nanoparticles loaded with TIMP-3 mRNA, with composition percentages expressed by total mass.

The hydrogel preparation protocol involves dissolving P407 and P188 in PBS at 18% and 4.5% (w/w), respectively, under high-speed stirring at 4 °C for at least 72 hours. For nanoparticle incorporation, it is essential to adopt gentle mixing techniques that minimize air entrainment and mitigate interfacial stress.

First, a 100% weight formulation was prepared to verify that the rheological properties of the hydrogel matched those previously obtained by the MiNt group and to assess its biocompatibility.

Then, a 90% weight formulation was prepared and subsequently completed to 100% by adding either pure water or nanoparticle suspension, to:

- 1. Investigate whether the addition of the remaining 10% of the total weight after Poloxamer dissolution, performed used a mixing method compatible with nanoparticles stability, affects the rheological properties of the hydrogel.
- 2. Compare the antitumor efficacy of the hydrogel-based delivery system with that of free TIMP-3 NPs.

The preparation process is illustrated in *Figure 16*. For both formulations, poloxamers were first weighed $(A.i \mid B.i)$ and combined with 10X PBS $(A.ii \mid B.ii)$. In the 100% weight hydrogel formulation (Fig. 2A), MilliQ water was then added to reach a final PBS concentration of 1X (A.iii), followed by stirring at 4 °C for 72 hours (A.iv). In the loaded hydrogel system (Fig. 16B), MilliQ water was added to reach 90% of the final weight (B.iii), then stirred under the same conditions (B.iv). The remaining 10% was subsequently added either as nanoparticle suspension or pure water (in the case of a bare hydrogel), reaching a final PBS concentration of 1X (B.v).

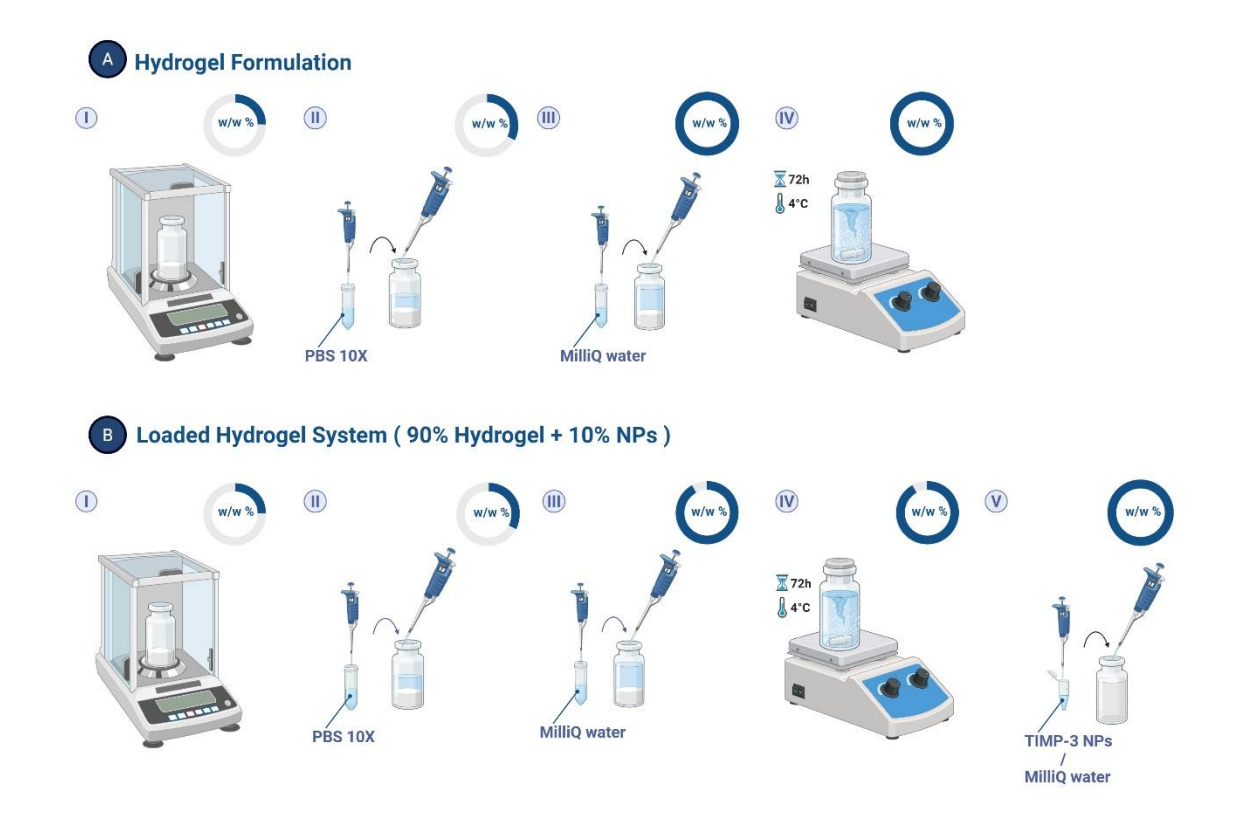


Figure 16: Schematic representation of the preparation process for the 100% hydrogel formulation (A) and the loaded hydrogel system (B). For each step (i-v), the pie charts indicate the fractional content (% w/w) of the system components at that specific stage. Created in https://BioRender.com

4.2 Characterization of the system

Rheological analysis

Rheological analysis was performed using a Discovery HR20 rheometer (TA Instruments) equipped with a cone plate geometry (diameter: 40 mm; angle: 0.995556 °). Measurements were conducted with a sample volume of 300 μ L and a plate gap of 27 μ m. The samples were loaded on the plate from a glass tube stored at 4 °C. Silicon oil was used to seal the cover plate after sample deposition.

G' (storage modulus) and the G'' (loss modulus), the elastic and viscous component, respectively, are defined in terms of the maximum amplitude of the stress (σ_0) , the maximum amplitude of the strain (γ_0) , $\omega=2\pi f$ (f= frequency), and the loss angle (δ) .

$$G' = \frac{\sigma_0}{\gamma_0} cos\delta$$
 $G'' = \frac{\sigma_0}{\gamma_0} sin\delta$

The loss factor $\tan \delta$ and the complex viscosity $|\eta^*|$ are defined as follows:

$$\tan \delta = \frac{G'}{G''} \qquad |\eta^*| = \frac{1}{\omega} \sqrt{G'^2 + G''^2}$$

Oscillatory strain sweeps at a constant frequency of 1 Hz were performed at 37 ° C to determine the linear viscoelastic region (LVR), defined as the range of strain amplitudes over which G' and G" remain constant. The strain amplitude was varied from 0,01% to 10,0%. To determine the gelation temperature, an oscillatory regime of deformation within the LVR (constant frequency of 1 Hz and constant strain amplitude of 0.1 %) was applied and G' and G" were measured as a function of temperature from 20 °C to 40 °C with a heating rate of 1°C/min. Finally, G' and G" were measured at 37°C as a function of oscillatory frequency (from 0.1 to 10 Hz) to determine the viscoelastic properties after gelation. All data were collected and analysed using TRIOS software (TA Instruments).

Scanning Electron Microscopy

Hydrogel samples, both empty and loaded with nanoparticles, were prepared for scanning electron microscopy (SEM) analysis using two different dehydration methods: lyophilization (freeze-drying) and oven drying (air drying). In the first case, the liquid samples were first incubated at 37 °C to allow gelation, then subjected to the integrated pre-freezing stage of the lyophilizer (stepwise cooling), followed by sublimation under vacuum. For oven drying, the samples were dried at 70 °C until complete dehydration was achieved. In both cases, the dried hydrogels were mounted on aluminium stubs and coated with a thin layer of conductive material prior to imaging.

4.3 In vitro cell viability studies

In order to evaluate the efficacy and safety of the proposed treatment, the following tests were performed: an indirect assessment of the hydrogel's biocompatibility and an evaluation of the anti-tumor efficacy of TIMP-3-loaded nanoparticles, including a comparison with a control nanoparticle formulation lacking therapeutic activity.

Cells at approximately 90% confluence were seeded in 96-well plates (100 μ L/well) at the following densities: B16-F1 and B16-F10 at 40,000 cells/mL, and melan-a at 125,000 cells/mL.

MTT assay

Cell viability was evaluated by measuring metabolic activity using the MTT assay. At the selected time points following incubations under the different experimental conditions, supernatant was removed, and MTT reagent (3-(4,5- dimethylthiazol-2-yl)-2,5- diphenyltetrazolium bromide)) was added at a final concentration of 0.5 mg/mL. After 1 hour of incubation at 37°C, MTT solution was discarded and replaced by dimethyl sulfoxide (DMSO) to dissolve the formed formazan crystals. Absorbance was measured at 570 nm using a Tecan Infinite® plate reader (software: i-Control 2.0.10.0), and results were expressed as a percentage relative to the control group. Five replicates were included for each experimental condition.

Evaluation of the biological effect of T3-NPs

Transfection with TIMP-3 or GFP nanoparticles was carried out 24 hours after cell seeding. The following mRNA concentrations were tested: 0.01, 0.06, 0.1, 0.6, 1, 6, and 10 $\mu g/mL$. A negative control containing only culture medium was also included. Cell viability was evaluated 24-, 48- and 72-hours post transfection.

Hydrogel biocompatibility assay

Hydrogel biocompatibility was assessed using an indirect assay, based on the collection and testing of the degradation supernatant. The hydrogel volumes were selected to achieve poloxamer concentrations in the incubation mixture corresponding to those cells would experience in a direct exposure scenario.

The volumes required for hydrogel formulations of previously tested mRNA doses were determined, along with the medium volumes needed to reach a total volume of 100 µL per well. From these amounts, the poloxamer concentration for each condition was estimated. Knowing that the hydrogel formulation contains a total of 22.5% poloxamer (P407/P188 ratio 4:1), for example, for the highest mRNA dose tested, the final poloxamer concentration in the well—after adding 20 µL of culture medium in a total volume of 100 μL —is 18%. Increasing volumes of hydrogel were incubated in a fixed volume of culture medium to achieve the poloxamer concentrations corresponding to the different conditions, while ensuring a comparable FBS concentration across all samples. The hydrogel was first sterilized via ultraviolet (UV) irradiation., and the required volumes were incubated at 37 °C for 1 hour to allow gelation. Equal volumes of supplemented culture medium were added on top of each sample. The preparation was then incubated at 37 °C for 8 hours, a time point corresponding to approximately 50% weight loss according to preliminary solubilization studies (results not published yet) Sampling before complete dissolution allowed the collection of degradation by-products representative of an early-to-intermediate phase, minimizing cumulative effects and temporal dilution. Following incubation, the supernatant was collected and used to culture cells plated 24 hours earlier. A negative control, consisting of fresh culture medium, was included for comparison. Cell viability was evaluated 24-, 48- and 72hours after exposure to the supernatant. Results are presented for each condition based on the poloxamer percentage defined by the hydrogel-to-medium ratio used in the preparation.

4.4 In vitro efficacy analysis

To evaluate the molecular and functional outcomes of TIMP-3 mRNA therapy, intracellular TIMP-3 protein expression was assessed by Western blot and MMP-9 concentrations were quantified by ELISA.

B16 F1 and B16 F10 cells were seeded in 24-well plates at a density of 180,000 cells/mL. Two plates were prepared for each cell line for sample collection after experimental conditions at 24 and 72 hours. Each condition—negative control (C-), GFP-loaded nanoparticles (GFP-NPs), TIMP-3-loaded nanoparticles (T3-NPs), hydrogel alone (H), and hydrogel with nanoparticles (H + NPs)—was tested in triplicate. Treatments were applied 24 h after cell seeding. Prior to application, hydrogel formulations were sterilized via UV irradiation.

For the GFP-NPs and T3-NPs conditions, the required volumes of freshly prepared nanoparticles to deliver 1.8 µg of mRNA per well were directly added to the culture medium. For the H + NPs system, the volume necessary to achieve 1.8 µg of mRNA per well was mixed with the hydrogel (90:10 H: NPs) and placed in individual Transwell inserts, above wells containing fresh medium. In the H condition, the Transwell insert received the same volume as in the H + NPs system, but consisting of the 100% hydrogel formulation, with medium refreshed in the well.

Sample preparation

Following 24 and 72 h incubations, the cell suspension was centrifuged at 4000 rpm for 10 minutes at 4 °C to isolate the pellet, which was then resuspended in 180 μ L of RIPA buffer supplemented with a protease inhibitor cocktail. Samples were subjected to two cycles of sonication (2 min) and freezing at -80 °C (5 min). Lysates were centrifuged at 14,000 rpm for 10 minutes at 4 °C, and the clarified supernatant was collected for analysis.

The total protein concentration was determined using the Thermo Scientific™ Pierce™ BCA Protein Assay Kit, employing a Bovine Serum Albumin (BSA) standard curve ranging from 25 to 2000 µg/mL (0 µg/mL used as blank). The working reagent was prepared at a 50:1 ratio of Reagent A to Reagent B, and 200 µL of the mixture were added to 20 µL of standards or samples. Supernatants were diluted 1:100 in PBS, while lysates were diluted 1:5 in PBS. The plate was then incubated at 37 °C for 30 minutes, and absorbance was read at 562 nm using a Tecan Infinite® plate reader. The processed samples were subsequently used for further analyses.

Western Blot for TIMP3 relative quantification

TIMP-3 protein levels were assessed by Western Blot, and the intensity of the TIMP-3 band was quantified relative to a housekeeping protein (β -actin). Intracellular protein samples were boiled at 95 °C for 10 minutes in 5X loading buffer supplemented with β -mercaptoethanol (1:20, v/v) as protein reducing agent. A total of 20 μ g of protein was separated on 12% SDS-PAGE gels, followed by electrotransfer onto PVDF membranes. Blocking was performed with 5% (v/v) non-fat milk in TBST (Tris-buffered saline with 0.1% Tween-20) for 1 hour at room temperature. Primary antibody incubation was performed overnight at 4 °C, using dilutions of 1:1000 for anti-TIMP-3 and 1:500 for anti- β -actin in blocking buffer. Following washing in TBST (three times, 10 min each), membranes were incubated with secondary antibodies (1:2500 dilution for anti-rabbit and 1:2000 for anti-mouse) for 40 minutes at room temperature. Chemiluminescence was revealed by adding HRP-TMB substrate and detected with the Amersham system.

ELISA for MMP-9 evaluation

MMP-9 protein concentration was determined using a commercial ELISA kit (ab100606, Abcam) following the manufacturer's instructions. Briefly, 50 μ L of each sample and 50 μ L of the provided Antibody Cocktail were added to the wells of a 96-well plate. The plate was covered with a sealer and incubated for 1 hour at room temperature with gentle orbital shaking. After incubation, the wells were aspirated and washed three times with 300 μ L of 1× Wash Buffer. Then, 100 μ L of TMB Development Solution were added to each well and incubated for 5 minutes in the dark with gentle shaking. Finally, 100 μ L of Stop Solution were added, and the optical density was measured at 450 nm using a microplate reader. Results are normalized by total protein concentration and with the total volume of supernatant.

5. Results

The suitability of the P407/P188 hydrogel formulation for the intended application was established under conditions relevant to handling, injection and in vivo residence. The relative efficacy of TIMP-3 NPs was compared to eGFP NPs across melanoma and control cell lines to identify selective antiproliferative effects. TIMP-3 intracellular levels and secret MMP-9 levels were assessed to understand TIMP-3 expression dynamics and its modulation of proteolytic signaling in melanoma.

5.1 Rheological analysis

To assess the thermo-mechanical behavior of the P407/P188 hydrogel formulation and its suitability for injectable, in situ gelling applications, rheological measurements were conducted to characterize its sol-gel transition, define the key thermal transition points and evaluate the viscoelastic stability of the gel after network formation. As a second objective, an NP-incorporation strategy—completing the formulation by manual pipetting of the final 10% (v/v)—was evaluated to assess its impact on gelation and batch-to-batch reproducibility.

Rheological characterization of the P407/P188 hydrogel formulation

Strain Sweep Test

Strain sweep analysis was performed to understand the mechanical properties of the formulation at room temperature and physiological temperature and to determine the linear viscoelastic region (LVR) and the yield point.

At 37 °C, the hydrogel displays a higher storage modulus than the loss modulus ($G' \approx 10,000 \text{ Pa}$; $G'' \approx 2,000 \text{ Pa}$; Figure 17). A well-defined LVR is observed, extending from low strain values up to about 1%. Beyond this point, the hydrogel network begins to yield, with G' progressively decreasing and eventually crossing over G'' (at approximately 5% strain), which marks the onset of network failure. Mechanistically, the applied strain disrupts the physical crosslinks between micelles responsible for gelation, leading to a transition to a predominantly viscous behaviour.

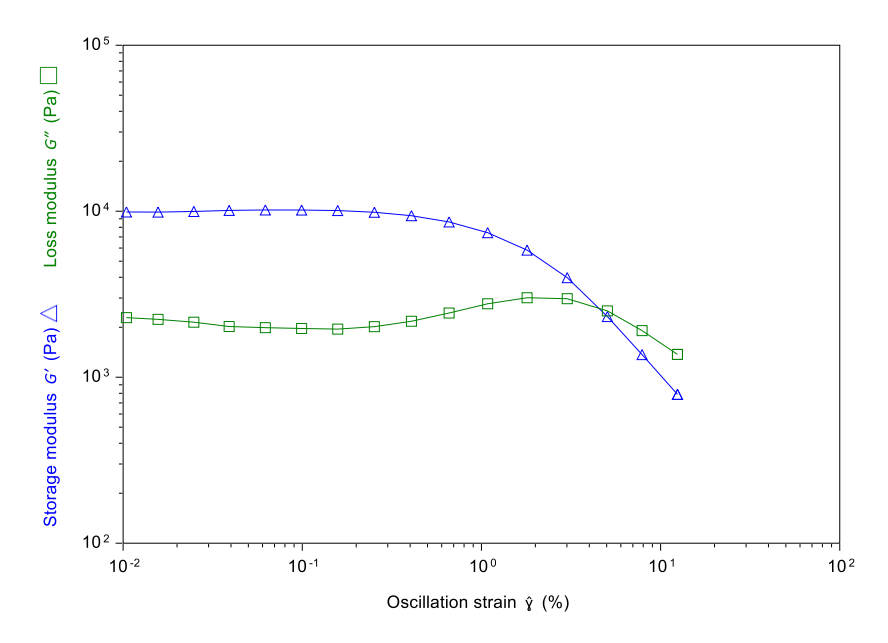


Figure 17: **Strain sweep at 37 °C**. Storage modulus (G', blue triangles) and loss modulus (G'', green squares) are reported as a function of oscillation strain (γ , %).

At 20 °C (Figure 18), both storage modulus (G') and loss modulus (G") are substantially lower than those measured at 37 °C. Across the explored strain range, G" exceeds G', indicating a sol-like state. In these conditions, a LVR is not identified. G" remains essentially strain-independent, whereas G' shows a slight initial increase followed by a progressive decrease with increasing strain. These observations suggests that at 20°C the polymer chains remain largely dissolved as unimers or form only loosely associated micelles that do not confer significant elastic strength to the formulation.

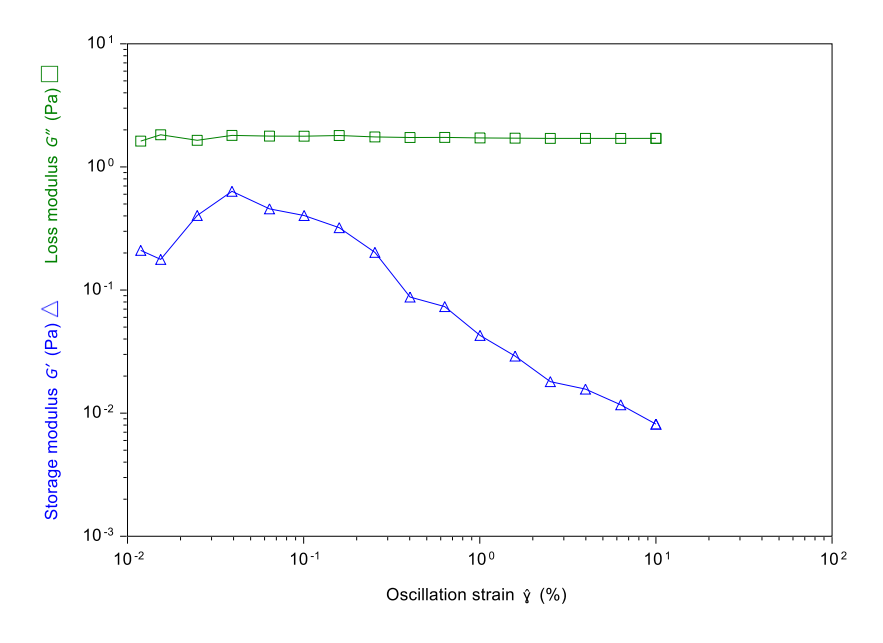


Figure 18: **Strain sweep at 20°C**. Storage modulus (G', blue triangles) and loss modulus (G'', green squares) are reported as a function of oscillation strain (γ , %).

Temperature sweep

An oscillatory temperature sweep between 20 °C (below the gelation threshold, as indicated by previous tests) and 40 °C was performed to record the storage and loss moduli as a function of temperature and identify the critical micelle temperature (CMT), the sol-gel transition temperature ($T_{\text{sol-gel}}$), and the temperature at which complete gelation occurs.

Figure 19 displays the dynamic heating temperature ramp (n=3). The observations are explained in terms of micellar organization, network formation, and temperature-dependent sol-gel transitions. At low temperatures, G'' is higher than G', indicating that the sample behaves as a viscous liquid. In this regime, the intrinsic storage modulus is very low, and the stress response generated under small-amplitude oscillatory strain approaches the lower detection limit of the rheometer. This led to disturbed G' measurements during early temperature ramp stages, which also reflects in the $\tan \delta$ plot. For graphical clarity, the phase angle (δ) was plotted instead of $\tan \delta$, while the discussion refers to $\tan \delta$, which directly expresses the ratio of viscous to elastic contributions.

With increasing temperature, dehydration of the PPO blocks promotes the self-assembly of spherical micelles. This structural rearrangement begins gradually: the onset of micelle formation is reflected in a gradual increase of the storage modulus (G') accompanied by a decrease in the loss tangent, though G' remains lower than G" at first. The critical micelle temperature (CMT) was observed at approximately 27 °C. As temperature continues to rise, micelles become sufficiently numerous and begin to pack into a network. At this stage, G' crosses over G" and tan δ drops below unity. The sol-gel transition temperature (Tsol-gel), generally defined by the point at which the loss tangent reaches unity, was around 29 °C. After the crossover point, both moduli continue to rise. With the increasing number of micelles, the material stores more elastic energy, while ongoing micelle-micelle interactions contribute to transient energy dissipation through rearrangements and dynamic bonding. Complete gelation is observed when both moduli reach a plateau, with G' > G" and tan δ remaining nearly constant. The gelation temperature was approximately 34 °C. The main transition points, together with the corresponding values of the storage modulus (G'), are summarized in Table 1.

Transition point/ Condition	Temperature (°C)	Storage modulus G' (Pa)	
Critical micelle temperature (CMT)	27.44 ± 0.55	0.18 ± 0.02 Pa	
Sol-gel transition (G'=G")	29.37 ± 0.41	3.28 ± 0.49 Pa	
Complete gelation	34.09 ± 0.16	7740.55 ± 149.86	
Physiological temperature	37.00	11763.03 ± 101.60	

Table 1: Characteristic transition temperatures and corresponding storage modulus (G') values of the P407/P188 reported as mean \pm SD (n = 3).

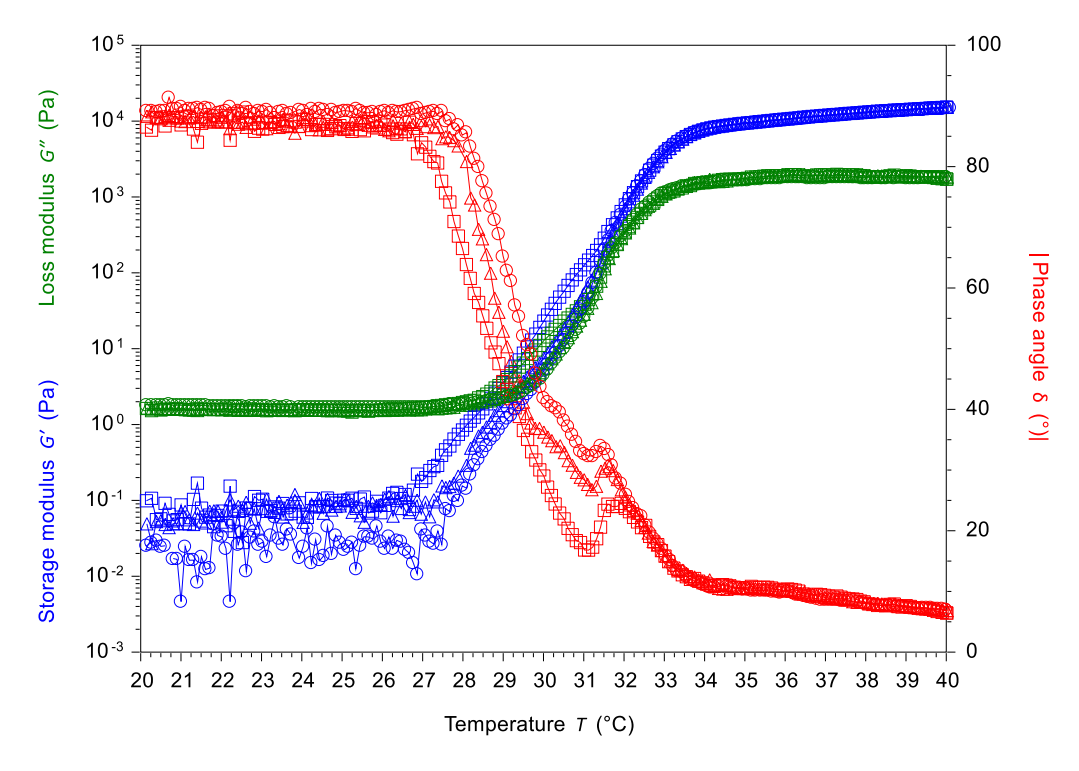


Figure 19: Temperature ramp at 1 °C/min. Storage modulus (G', blue), loss modulus (G'', green), and phase angle (δ , red) as a function of temperature.

Frequency sweep

Frequency-sweep measurements allow to quantify the dependence of the storage and loss moduli on angular frequency, helping predict the material's behavior in situ.

At 37 °C, the frequency sweep confirms that the hydrogel exhibits a solid-like behavior, with G'>G" (Figure 20). The storage modulus remains essentially frequency-independent, while the loss modulus shows a gradual decrease, indicating reduced viscous dissipation at higher frequencies. This behavior reflects a well-developed micellar network capable of maintaining its structural integrity under dynamic conditions.

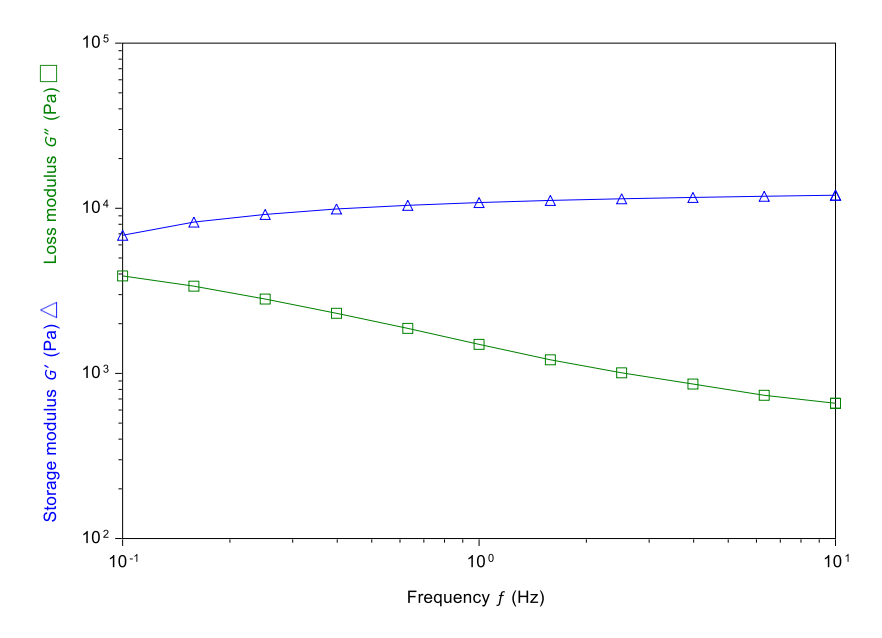


Figure 20: **Frequency sweep at 37 °C.** Storage modulus (G', blue triangles) and loss modulus (G'', green squares) as a function of angular frequency.

The rheological stability of the formulation was assessed for T_{sol→gel}, T_(gel), viscosity, and viscoelastic properties after one week of storage at 4 °C. No significant differences were observed between the initial data and the stored formulations (Figure 21).

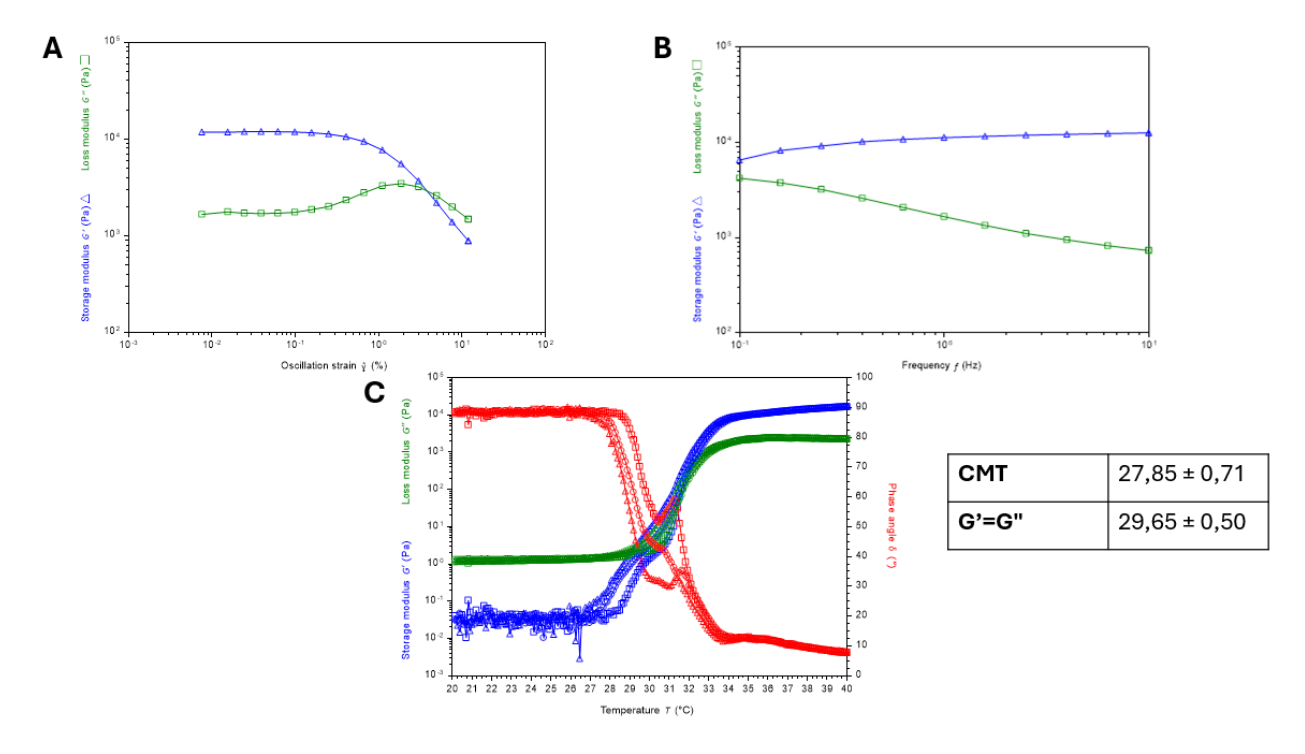


Figure 21: **Rheological characterization of the hydrogel after one week of storage at 4 °C**. (A) Strain sweep at 37 °C. (B) Frequency sweep at 37 °C. (C) Temperature ramp at 1 °C/min, with reported critical micelle temperature and sol–gel transition temperature.

The rheological characterization confirms that the hydrogel is suitable for in vivo application. The sol-gel transition temperature is sufficiently above room temperature to ensure that the formulation remains in a low-viscosity sol state during handling and

injection. Complete gelation occurs close to, but below, body temperature, ensuring in situ gel formation at the injection site. The mechanical strength of the hydrogels is essential for maintaining their integrity in the body. Tumor tissues can expand as they grow and undergo cell contraction as well [93]. The frequency sweeps results suggest that the hydrogel can withstand tumor-related movements without undergoing structural failure. However, in vitro-released studies provided evidence of low gel strength: as a consequence of rapid erosion, the system displayed a burst release profile, characterized by the fast release of a considerable fraction of the payload in PBS at 37 °C.

Other parameters such as the gelation time, injectability and the impact of sterilization on mechanical integrity and rheological behaviour should be considered for the desired application. Gelation time could be evaluated performing a time sweep at constant frequency and strain. Injectability can be quantitatively assessed by measuring the extrusion force required to expel the formulation from a syringe using a texture analyser, under controlled temperature conditions and with clinically relevant needle gauges[94]. While clinical use of poloxamers typically relies on steam sterilization by autoclaving – and several studies have investigated its impact on rheological properties[95], [96], [97]–in this study UV exposure was adopted as a practical, non-thermal method of sterilization suitable for preliminary in vitro cytotoxicity testing. For clinical translation, however, it will be essential to establish an optimal sterilization protocol that ensures both sterility and preservation of hydrogel performance.

While rheological measurements provide direct insight into the viscoelastic changes of the system, complementary techniques are required to validate the identified CMT and to characterize the transition between different micelle packing geometries (e.g., from a disordered arrangement to more ordered cubic or face-centered cubic structures). Differential scanning calorimetry (DSC) can detect endothermic peaks associated with PPO dehydration, which corresponds closely to the onset of micellization [98], [99]. Dynamic light scattering (DLS) can show the presence of unimers, micelles, and clusters of micelles and reveal changes in micelle size as temperature increases. CMT can be identified where changes in light scattering intensity indicate the onset of micelle aggregation [98], [99]. Small-angle X-ray scattering (SAXS) provides direct structural information on the internal organization of micelles, enabling the identification of their size, shape, and lattice arrangement [99], [100], [101].

Loading Strategy: Effect of Final 10% (v/v) Water Addition on Gelation and Reproducibility

Following assessment of the formulation's suitability for the intended application, the feasibility of NP incorporation through a final manual-pipetting step was investigated by completing the formulation with a water-only (mock) 10% (v/v) addition, and the resulting impacts on mechanical properties and gelation behavior were evaluated.

Figure 22 compares the strain sweep tests performed at 37 °C for the 100% hydrogel formulation (Fig. 22A) and for the sample prepared at 90% and subsequently completed to 100% by gentle manual pipetting of the remaining 10% volume (Fig. 22B). Lissajous curves are also shown at three characteristic points: within the LVR (0.1% strain), at the crossover point (G' = G''), and at the end of the analysis. At small deformations (0.1% strain), the sample prepared at 90% + 10% water displayed a wider ellipse, consistent with its higher tan δ (0.46 vs. 0.20 for the 100% formulation). The yield stress was also lower for the 90% + 10% water sample (\approx 3% strain) compared with the 100% hydrogel (\approx 5% strain).

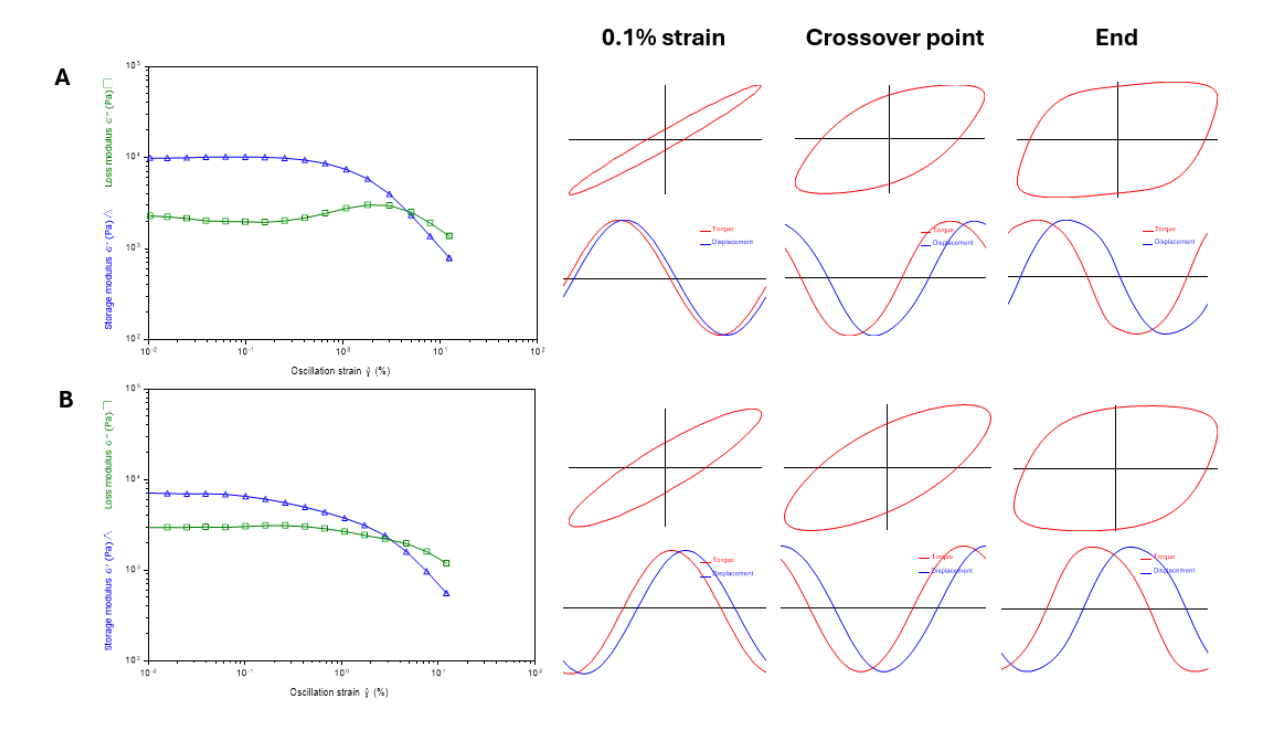


Figure 22: Strain sweep analysis and Lissajous curves of the 100% hydrogel formulation (A) and the 90% hydrogel + 10% water formulation (B), both tested at 37 °C.

A temperature ramp test (n = 3) was carried out after determining the LVR to assess whether adding the final 10% of water after poloxamer dissolution affects the gelation behavior. Since evident differences were observed among the three replicates, the results are presented and discussed separately.

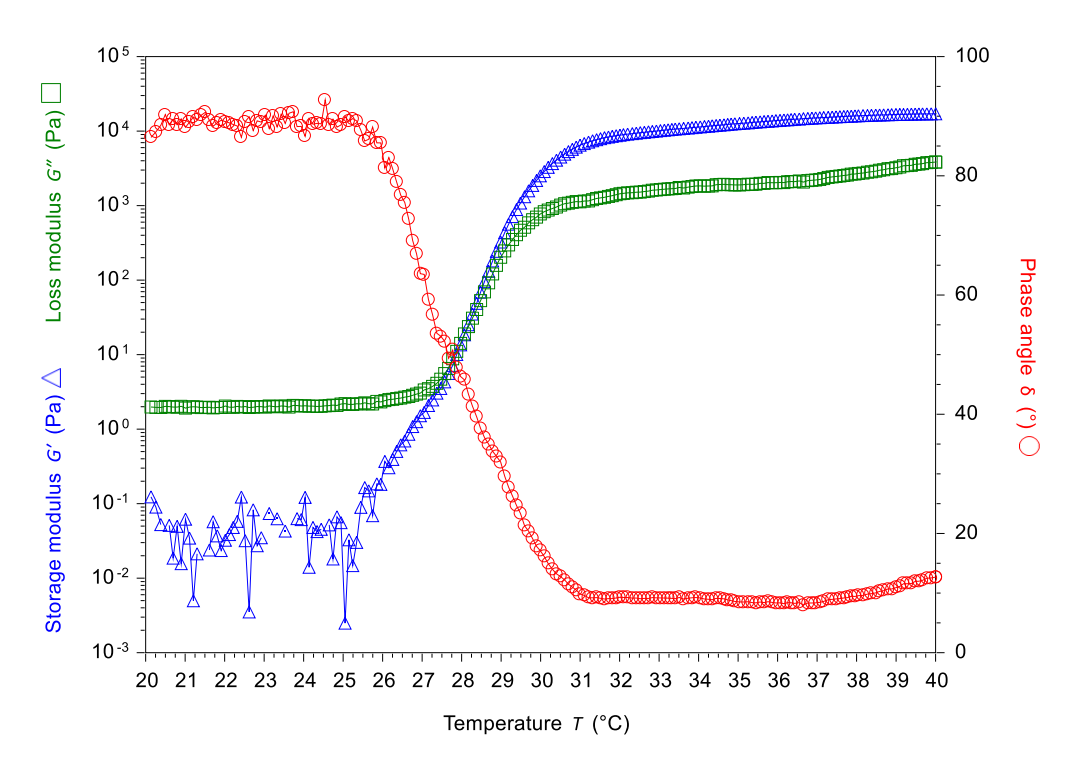


Figure 23: **Temperature ramp test of the 90% formulation + 10% water (replica 1).** Storage modulus (G', blue), loss modulus (G'', green), and phase angle (δ , red) as a function of temperature

As shown in Fig. 23, during the initial phase of the temperature ramp, G'' exceeds G', indicating that the polymers are present mainly as unimers or loosely associated micelles. The CMT was identified at approximately 26 °C ($G' \approx 0.2$ Pa), while the sol–gel transition occurred around 28 °C, where G' reached ~20 Pa—nearly one order of magnitude higher than in the 100% formulation. Complete gelation occurred at approximately 31 °C.

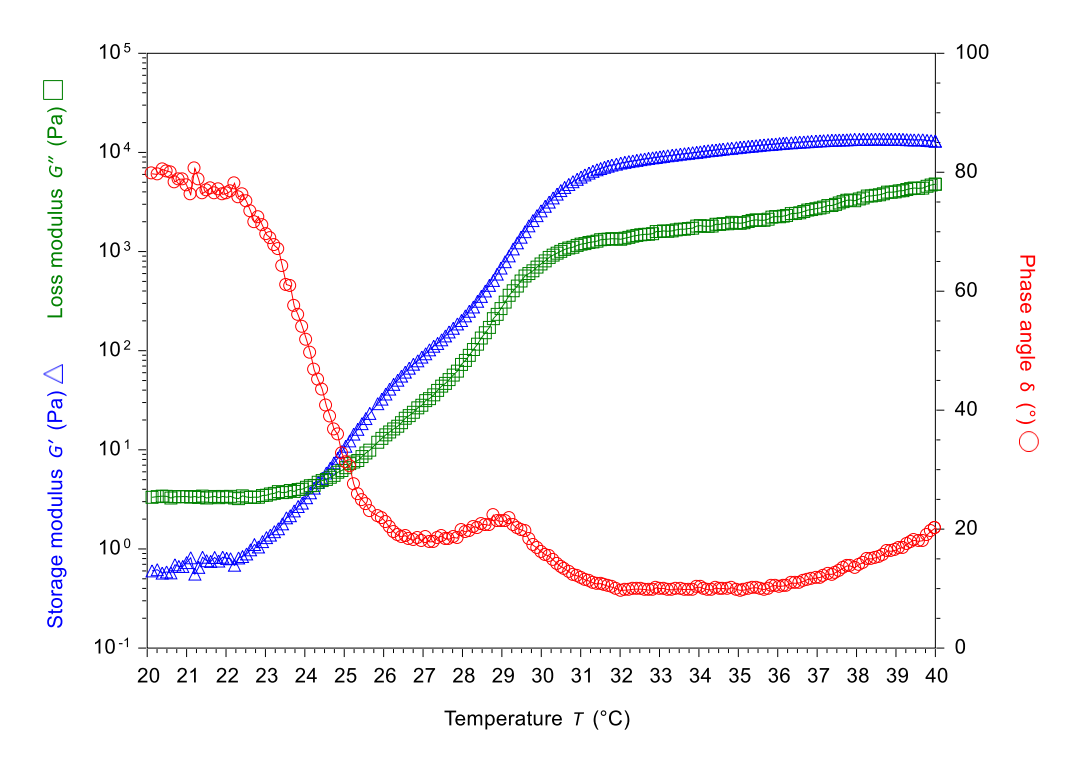


Figure 24: **Temperature ramp test of the 90% formulation + 10% water (replica 2).** Storage modulus (G', blue), loss modulus (G', green), and phase angle (δ , red) as a function of temperature

In the replicate shown in Fig. 24, the region in which G" > G' is less extended and G' started at a higher value than in the previous replicate. The CMT was observed at approximately 23 °C (G' ≈ 1 Pa), and the crossover point was identified shortly after at ~24 °C (G' ≈ 5 Pa). Complete gelation was observed at approximately 32 °C.

Finally, in Fig. 25, the sample was already in the gel state at the beginning of the test (20 °C), as indicated by G' > G'' from the start. This observation suggests that both the CMT and $T_{sol \rightarrow gel}$ occurred below 20 °C, preventing their direct identification within the tested temperature range. Complete gelation was observed at approximately 29 °C.

Despite the differences observed among replicates, the storage modulus at 37 °C was comparable across all tests and consistent with the value measured for the 100% formulation.

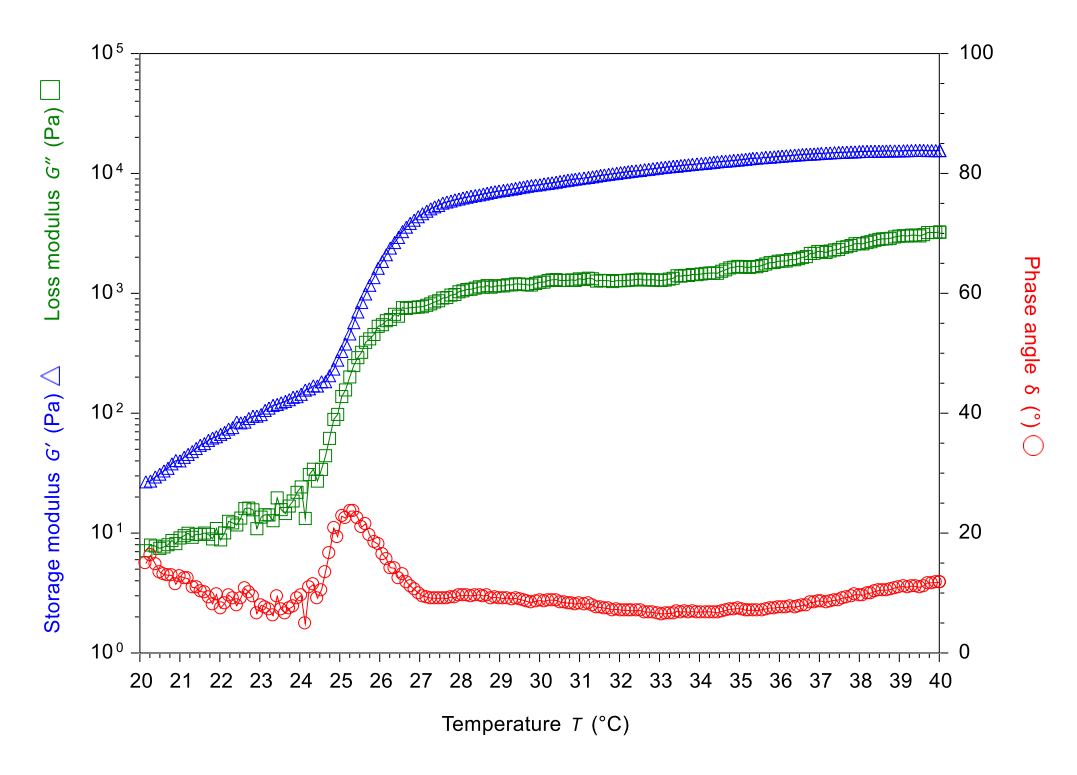


Figure 25: **Temperature ramp test of the 90% formulation + 10% water (replica 3).** Storage modulus (G', blue), loss modulus (G'', green), and phase angle (δ , red) as a function of temperature

Before the final 10% addition (water or NP suspension), the hydrogel corresponded to a "90% solution" in which the polymer and buffer concentrations are transiently higher than in the final formulation. Specifically, the concentrations are approximately 20% (w/w) for P407 and 5% (w/w) for P188. Similarly, since PBS 10X is diluted only up to 90% of the final volume, its concentration at this stage is higher than 1X. Rheological analysis showed that completing the formulation by manual pipetting of the remaining 10% volume resulted in incomplete mixing. Since the sol–gel transition of poloxamer-based hydrogels is highly dependent on polymer concentration, uneven dilution could produce region-specific differences in polymer hydration, influencing both the initial state of the hydrogel and its subsequent response to temperature changes, as evidenced by the analysis.

Additional studies are needed to evaluate how mixing methods affect nanoparticle stability, aggregation and mRNA cargo leakage. A DLS temperature ramp and salt-concentration ramp could clarify the role of poloxamer and PBS concentration in this protocol and support the definition of an adequate mixing strategy.

For the application of the hydrogel as carrier for intratumoral injection, the reproducibility of the gelation process is paramount. However, for the purposes of the cell culture experiments, the key parameter is the mechanical stability of the gel at physiological temperature. Since the storage modulus at 37 °C was unchanged when comparing the 100% formulation with the 90% formulation + 10% water, the 90% hydrogel + 10% NPs system was employed in this study to assess whether embedding NPs provides sustained release and a time-dependent uptake/response, in contrast to free NPs.

5.3 Scanning Electron Microscopy Characterization

The dehydration process required for SEM analysis alters the physical state of hydrogels and introduces artifacts that do not reflect the true structure of the hydrogel in its native form. Moreover, poloxamer hydrogels are known for their sensitivity to drying conditions – largely due to their amphiphilic nature and the formation of micellar networks that are stabilized by water. The influence on oven and lyophilization drying on the resulting SEM images in terms of network morphology, porosity, and artifact formation was analysed.

In the case of the oven drying protocol, the volumetric shrinkage induced by water evaporation generates high capillary and tensile stresses at the solid-liquid interfaces. Once these stresses overcome the structural integrity of the hydrogel, structural failure occurs through the formation of cracks, which are clearly visible in Figure 26A (empty hydrogel) and 26B (hydrogel loaded with NPs).

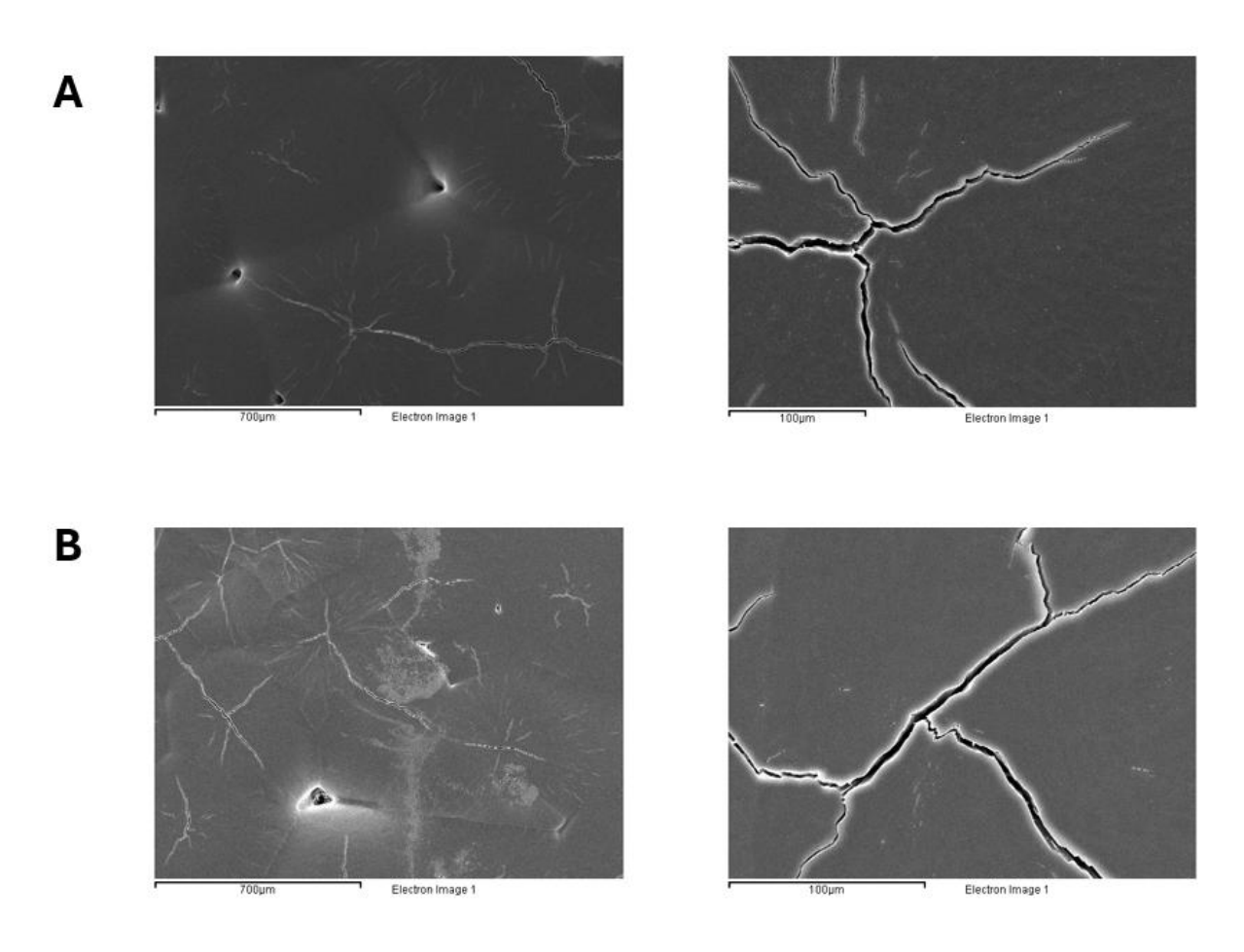


Figure 26: **SEM micrographs of oven-dried hydrogels**. (A) Empty hydrogel. (B) Hydrogel loaded with nanoparticles. For both samples, an image at lower magnification (scale bar = $700 \mu m$) and a focus at higher magnification (scale bar = $100 \mu m$) are reported. Cracks are evident in both conditions as a consequence of dehydration-induced shrinkage and capillary stresses.

During dehydration, water removal concentrates the dissolved ions. Once their solubility limit is exceeded, they precipitate as crystals, which appear as artifacts in SEM micrographs. Salt deposits were observed on the surface of both the empty and the loaded hydrogel. In the loaded sample (Figure 27B. i), the crystals appeared smaller and more homogeneously distributed, in contrast to the larger and more aggregated deposits found in the empty hydrogel (Figure 27A.i).

In the case of the empty hydrogel (Figure 27A. ii), the EDS spectrum acquired from the crystalline deposits displays peaks corresponding to sodium (Na), chloride (CI), phosphorus (P) and potassium (K), confirming the presence of PBS-derived salts crystallized during the dehydration process. Gold (Au) signals originate from the gold sputter coating applied to ensure sample conductivity for SEM analysis. For the loaded hydrogel, two different EDS spectra were acquired from the same region (Figure 27B. ii), revealing the formation of mixed organic-inorganic regions instead of a phase separated salt domain as observed in the other case. In one spectrum a carbon (C) peak was detected, which may indicate co-precipitation processes or arrested phase separation. Sucrose can interact with ions via hydrogen bonding, thereby affecting ions diffusion and local supersaturation dynamics. This interpretation is supported by the absence of a phosphorus peak and by the relative attenuation of the oxygen peakassociated with phosphate deposits—compared with the spectrum of the bare hydrogel. The second spectrum, lacking carbon but showing attenuated Na and Cl signals, is consistent with the presence of arrested salt nuclei, suggesting incomplete or inhibited crystallization.

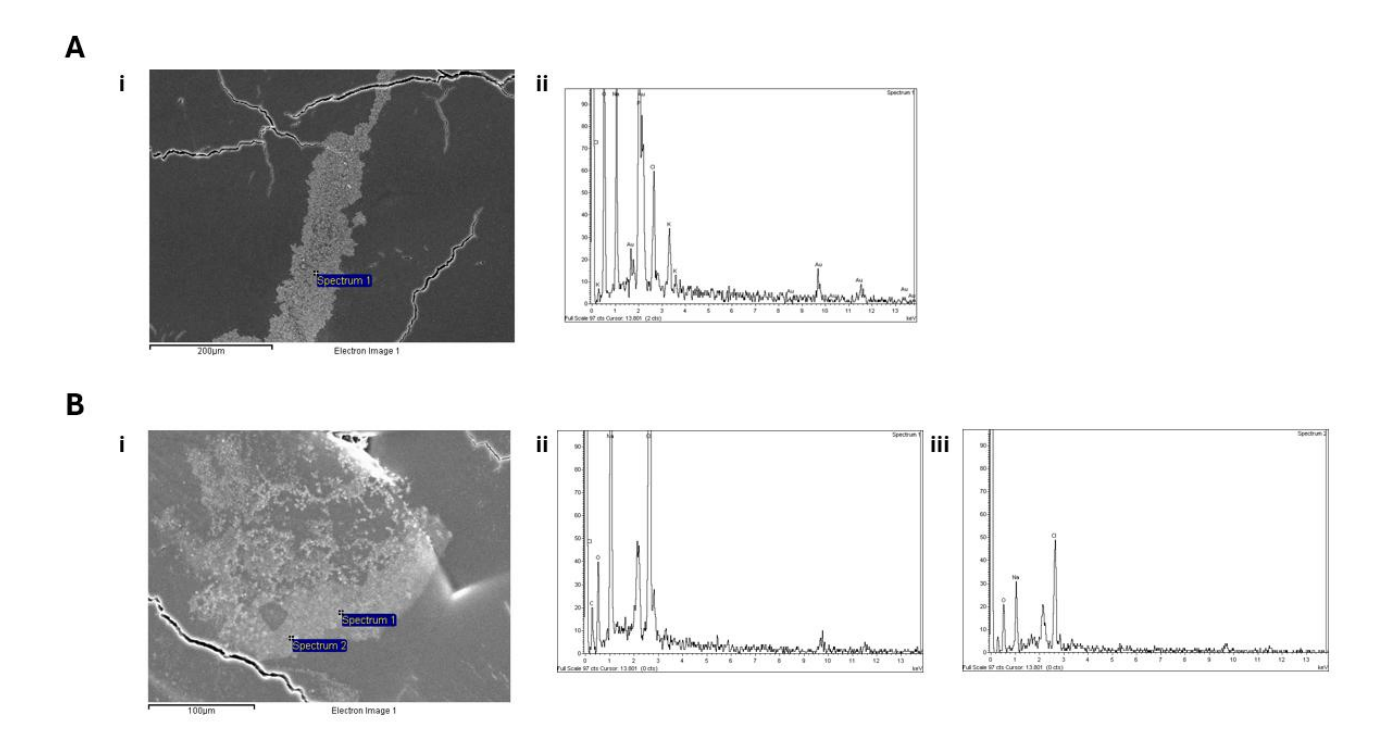


Figure 27: **SEM** micrographs and corresponding EDS spectra of crystalline deposits of oven-dried hydrogels. (A) Empty hydrogel (scale bar = $200 \,\mu\text{m}$). B) Hydrogel loaded with nanoparticles (scale bar = $100 \,\mu\text{m}$). In both cases, EDS spectra confirm the presence of PBS-derived salts (Na, Cl), while Au peaks originate from the gold sputter coating

Freeze-drying involves removal of water by sublimation from a previously frozen liquid solution. Although the samples underwent the same conditions during the dehydration process, SEM micrographs reveal distinct morphological differences. In the case of the empty hydrogel, irregular pores accompanied by salt deposits were observed, whereas in the loaded hydrogel pores appear smaller, more circular and more evenly distributed across the surface. During freezing, ice crystals grow while dissolved salts are excluded from the ice lattice and concentrated in the surrounding liquid. These salt-enriched domains constitute eutectic regions, confined within the interstitial spaces between ice and the polymer matrix, where the freezing point is locally depressed. Upon freezedrying, the pure ice regions sublimate into the vapor phase, whereas the less volatile eutectic domains remain in the dried hydrogel as crystalline residues [102], [103]. These appears on SEM (Figure 28A), where the EDS spectrum displays peaks of Na, Cl, and P, confirming the PBS-derived origin of these deposits. The detection of carbon further indicates their close association with the polymer matrix.

Such eutectic artifacts were not detected in the freeze-dried loaded hydrogel (Figure 3B), most likely due to the cryoprotective effect of sucrose, which modulates the kinetics of ice nucleation and growth. By increasing the viscosity of the aqueous phase, sucrose favors vitrification over crystallization, thereby suppressing the formation of large ice domains [104] and preventing the expulsion and local segregation of salts into interstitial regions.

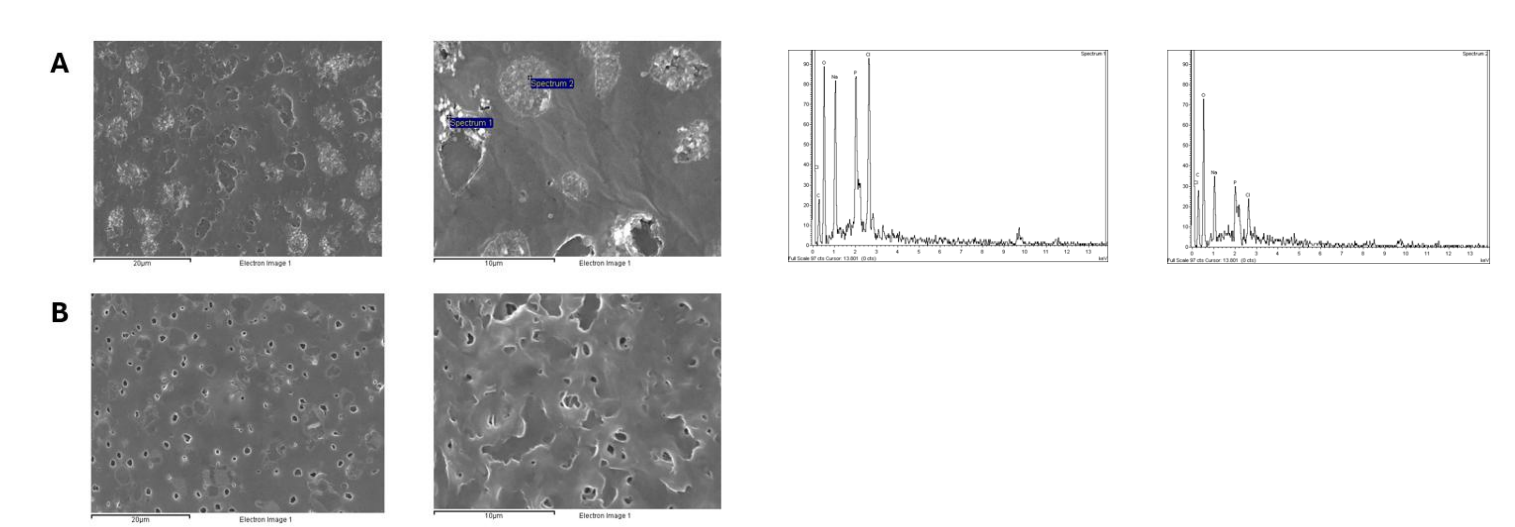


Figure 28: **SEM** micrographs of freeze-dried hydrogels. (A) Empty hydrogel. (B) Hydrogel loaded with nanoparticles. For both samples, images are shown at two different magnifications (scale bars: 20 μm and 10 μm). For the empty hydrogel, EDS spectra acquired from crystalline regions are also reported.

As discussed, the two applied drying techniques result in different morphological artifacts. Oven drying leads to significant shrinkage and densification of the hydrogel network, with SEM images showing aggregated pseudo-spherical structures and reduced porosity. The resulting morphology does not accurately reflect the native pore architecture, as extensive dehydration and heat cause collapse of the hydrogel network. In freeze-dried samples, as the ice sublimates, the spaces previously occupied by the crystals appear as pores. However, these are secondary features introduced during sample preparation and do not reflect the native hydrogel architecture [105], [106].

SEM data can still be used in a comparative manner, provided that all samples are subjected to the same preparation-induced artifacts. However, in oven-dried samples the presence of sucrose in the nanoparticle-loaded hydrogel alters the morphology, spatial distribution, and stoichiometry of the crystalline deposits. In freeze-dried samples, sucrose contained in the loaded formulation modulates ice nucleation and growth, thereby preventing the formation of salt deposits. In the bare hydrogel, where sucrose is absent, the uncontrolled growth of large ice crystals can also impose mechanical stress on the polymeric matrix.

A further limitation of the protocol adopted in this study is that SEM evaluation only reveals surface morphology, which does not accurately represent the internal pore architecture. Consequently, no reliable information on the true porosity of the hydrogels could be obtained.

For the above-mentioned reasons, these analyses did not yield a morphological characterization of the hydrogel but lead to the conceptualization of an optimized protocol for SEM sample preparation. Freeze-drying emerged as the most suitable approach; however, the stepwise cooling adopted in this protocol promotes the formation and growth of ice crystals, a process that alters the microarchitecture and drives the segregation of PBS salts into eutectic domains. Therefore, plunge freezing should be preferred. Importantly, the present results also demonstrate that the addition of a cryoprotectant such as sucrose can substantially reduce the step-down cooling-induced artifacts. An optimized protocol should additionally incorporate a step to expose cross-sectional surfaces, and sucrose should also be included in bare hydrogels to enable reliable comparisons.

Further characterization may employ techniques such as cryo-scanning electron microscopy (Cryo-SEM), which enable imaging of the sample in a cryogenically preserved state, and environmental scanning electron microscopy (ESEM), that allows the observation of samples in their native hydrated state.

It should be noted that freeze-drying in this study was performed solely to enable SEM analysis. In cases in which this procedure is required for storage purposes the effect of buffers on the protective mechanism afforded by sucrose should be taken into account [107].

5.4 In vitro cell viability studies

MTT assay

The therapeutic profile of TIMP-3 NPs was systematically characterized, with emphasis on efficacy and safety endpoints. The findings were used to articulate a data-driven hypothesis of its mechanism of action.

Dose–response curves were generated by evaluating metabolic activity through MTT assay following exposure of cells to increasing concentrations of eGFP mRNA and TIMP-3 mRNA (Figure 29). The half maximal inhibitory concentration (IC_{50}), representing the concentration of the tested formulation required to reduce cell viability or proliferation by 50% relative to untreated controls [108], was determined in GraphPad Prism using least–squares regression analysis.

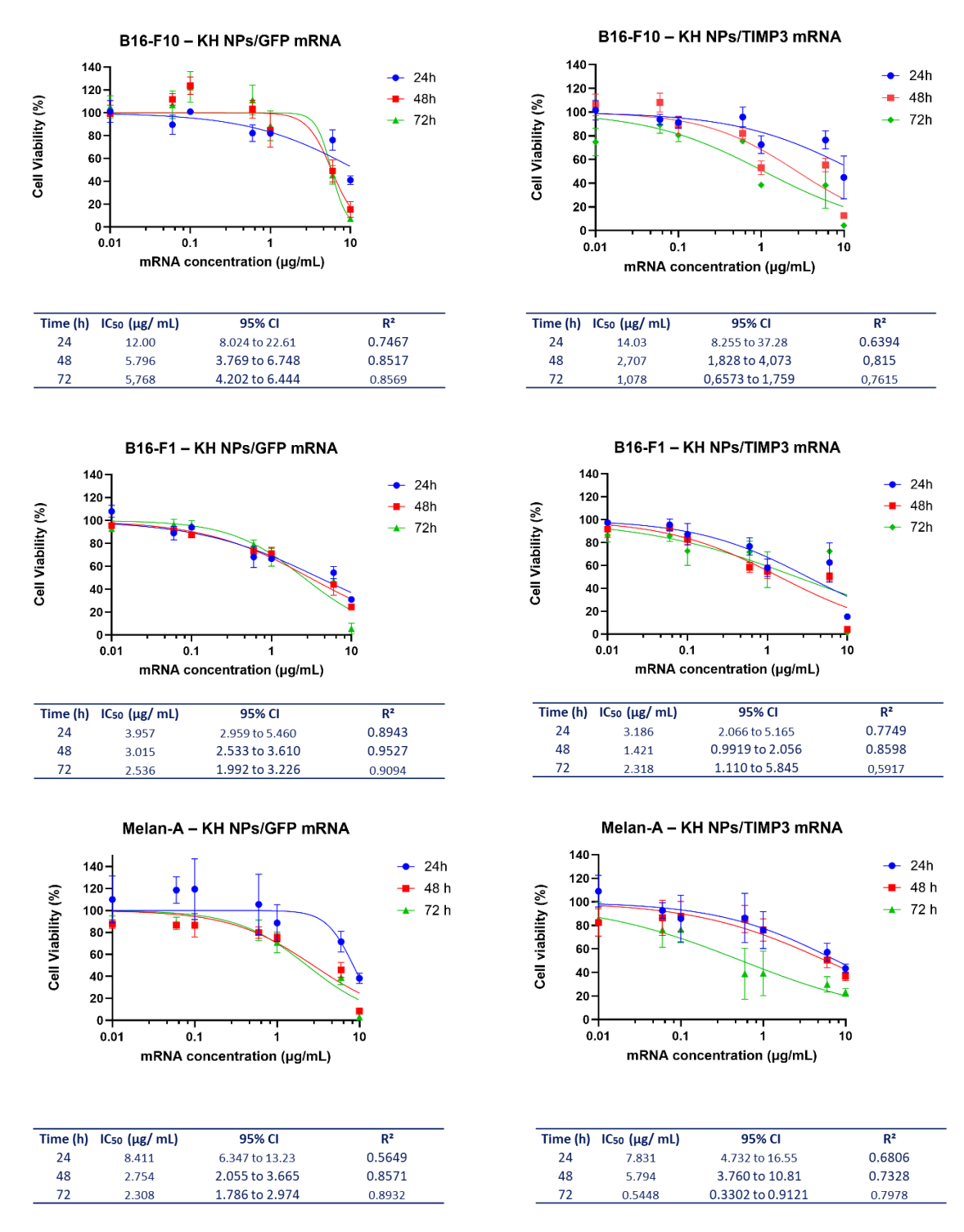


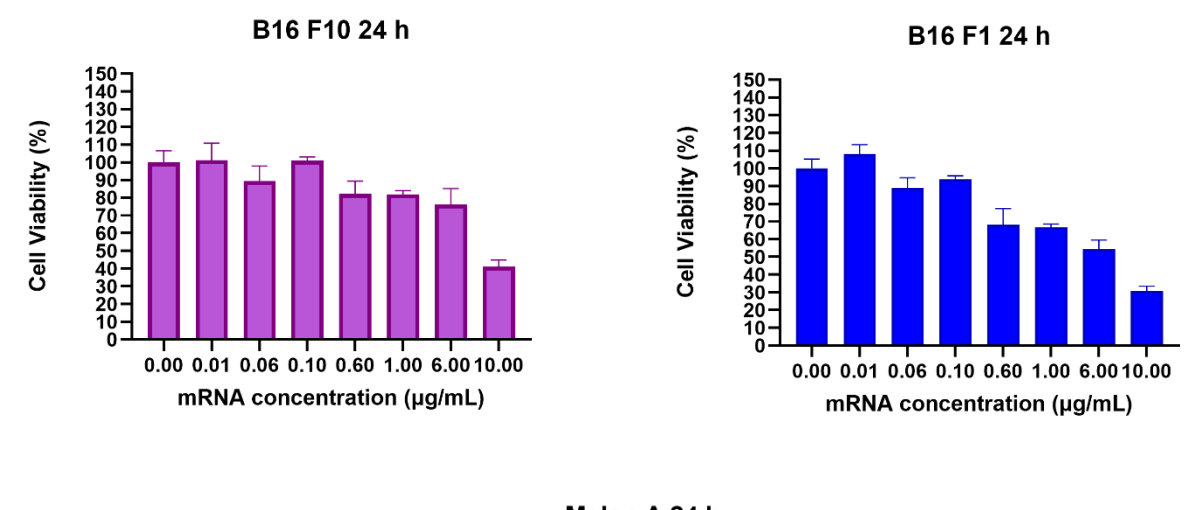
Figure 29: **Cytotoxic effect of KH nanoparticles (KH NPs) loaded with GFP or TIMP3 mRNA on murine cell lines**. The panels show the results for B16-F10 (top), B16-F1 (middle), and Melan-A (bottom) cells treated with KH NPs loaded with GFP mRNA (left) or TIMP3 mRNA (right). IC50 values (µg/mL), 95% confidence intervals, and R² values are reported in the tables below each graph.

For almost all the dose-response curves analysed, the coefficient of determination (R^2) did not exceed 0.9, indicating that the fit does not fully capture the experimental data. Consequently, the calculated IC₅₀ values should be regarded as approximate estimates,

a conclusion further supported by the wide confidence intervals observed in some cases. In addition, the dataset lacks measurements in the 1–6 μ g/mL range, which corresponds to the region where most IC₅₀ values are located; this gap may therefore have contributed to the uncertainty in their estimation.

KH NPs cytotoxicity

To assess the potential cytotoxicity of the carrier, cell viability was first analysed at 24 h across the tested concentrations (Figure 30A–C). A significant reduction in viability compared to the control, falling below the 70% threshold, was detected only at the highest concentration (10 μ g/mL) in B16–F10 and Melan–A cells, whereas in B16–F1 cells the effect, even if modest, was already evident from 1 μ g/mL. To further examine whether cytotoxicity was affected by exposure time, viability was compared across different time points at the same concentration.



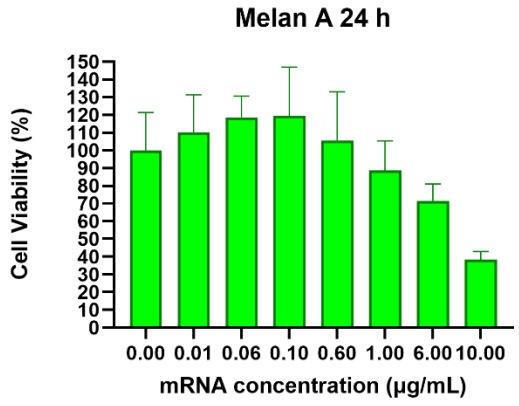


Figure 30: Cell viability at 24 h following treatment with eGFP-loaded nanoparticles (GFP-NPs). Histograms show the percentage of viable cells relative to untreated controls in (A) B16-F10, (B) B16-F1, and (C) Melan-A cells. Data are expressed as mean \pm SD (n = 5).

Significant reductions were detected only at 6 and 10 µg/mL, as shown in the curves reported in Figure 29, indicating that a delayed cytotoxic effect emerges only at higher concentrations.

For subsequent assays, cells were treated with 3 µg/mL, a concentration that remained above the 70% viability threshold in Melan-a cells at 72 h.

Efficacy of the proposed treatment

To assess whether there was a significant difference in cell viability between control (eGFP) and TIMP-3 treatments at each concentration, for each cell line, data were analysed using Welch's t-test. p-values were subsequently adjusted with the Holm - Sidak method (α = 0.05) to control the overall Type I error rate across the multiple comparisons. Only differences that remained significant after Holm-Šidák correction were considered statistically relevant, as summarized in table 2.

Cell line	Time (h)	Concentration (µg/mL)	Significance (uncorrected)	Significance (adjusted)	Effect observed
B16 F10	48	0.1	***	***	TIMP-3 ↓ viability vs eGFP
		0.6, 1	**	*	TIMP-3 ↓ viability vs eGFP
	72	0.01	**	*	TIMP-3 ↓ viability vs eGFP
		0.1	**	**	TIMP-3 ↓ viability vs eGFP
		0.6	**	*	TIMP-3 ↓ viability vs eGFP
		1	***	**	TIMP-3 ↓ viability vs eGFP
B16 F1	48	0.6	***	**	TIMP-3 ↓ viability vs eGFP
		1	**	*	TIMP-3 ↓ viability vs eGFP
		10	***	***	TIMP-3 ↓ viability vs eGFP
	72	0.06	**	*	TIMP-3 ↓ viability vs eGFP
		6	***	***	eGFP ↓ viability vs TIMP-3
Melan-a	48	10	***	***	eGFP ↓ viability vs TIMP-3
	72	10	***	***	eGFP ↓ viability vs TIMP-3

Table 2: Summary of statistical comparison of the effects of TIMP-3 mRNA versus GFP mRNA on cell viability. The table reports only those concentrations where significant differences in viability were observed, including both uncorrected and $Holm-\check{S}id\acute{a}k$ -adjusted significance levels, and specifies which treatment (TIMP-3 or GFP mRNA) was responsible for the reduction. (Significance levels: *p < 0.05; **p < 0.01; ***p < 0.001; ****p < 0.0001)

At 24 h, no significant differences were observed between TIMP-3 and GFP across the tested concentrations in any of the cell lines. In B16-F10 cells, at 48 h TIMP-3 treatment significantly reduced viability compared with GFP at concentrations from 0.1 to 1 μ g/mL, while no differences were observed at the highest doses (Figure 13A). At 72 h, the effect of TIMP-3 was more pronounced, with significant reductions already detected at 0.01 μ g/mL and persisting up to 1 μ g/mL (Figure 13B).

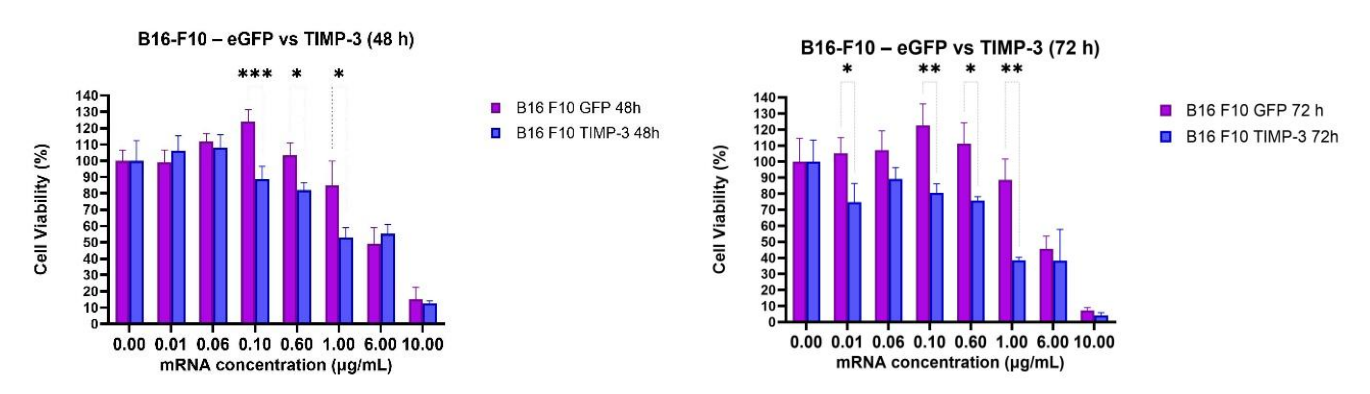


Figure 31: Effect of TIMP-3 mRNA treatment on B16-F10 cell viability. (A) 48 h; (B) 72 h. Data are presented as mean \pm SD (n=5). Statistical significance was determined by Welch's t-test with Holm-Šidák correction (*p < 0.05, **p < 0.01, ***p < 0.001)

In B16 F1 cells, TIMP-3 reduced viability at 48 h, with significant effects at 0.6, 1 μ g/mL and 10 μ g/mL (Figure 32A). At 72 h this outcome was attenuated: only a modest reduction was observed at 0.06 μ g/mL, whereas at higher concentrations viability of TIMP-3-treated cells was comparable to or even higher than that of GFP controls (notably at 6 μ g/mL, Figure 32B).

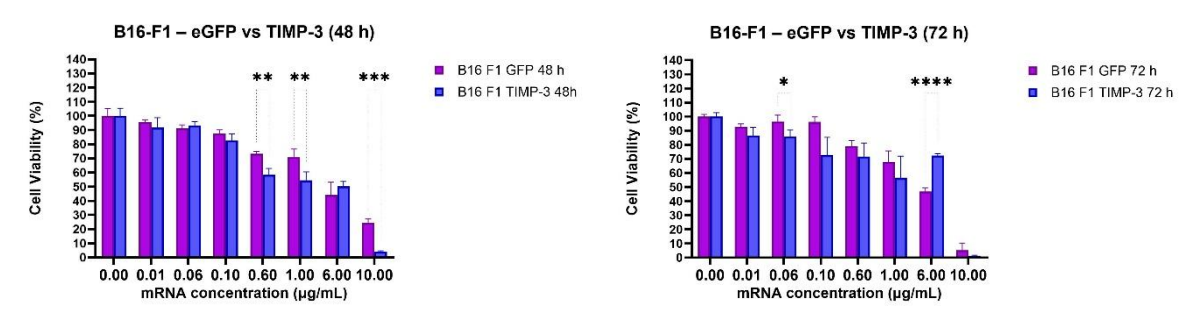


Figure 32: **Effect of TIMP-3 mRNA treatment on B16-F1 cell viability**. (A) 48 h; (B) 72 h. Data are presented as mean \pm SD (n=5). Statistical significance was determined by Welch's t-test with Holm-Šidák correction (*p < 0.05, **p < 0.01, ***p < 0.001)

In Melan-a cells, a trend toward reduced viability upon TIMP-3 treatment was visible only at 72 h, particularly at 0.6 and 1 μ g/mL (Figure 33B). Although these differences did not remain statistically significant after Holm-Šidák correction due to high variability among TIMP-3 replicates, the trend may still be biologically relevant given that Melan-a cells model healthy melanocytes. At both 48 h (Figure 33A) and 72 h (Figure 33B), a consistent significant effect was observed only at 10 μ g/mL, where GFP-treated cells showed lower viability compared with TIMP-3.

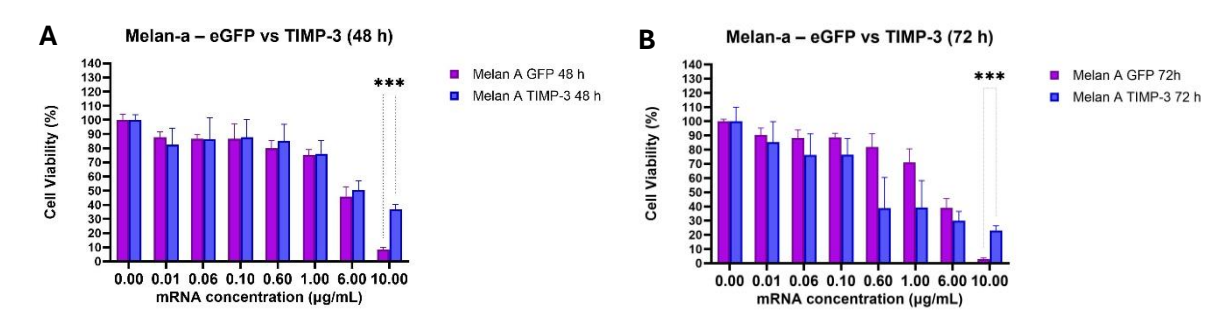


Figure 33: **Effect of TIMP-3 mRNA treatment on melan-a cell viability**. (A) 48 h; (B) 72 h. Data are presented as mean \pm SD (n=5). Statistical significance was determined by Welch's t-test with Holm-Šidák correction (*p < 0.05, **p < 0.01, ***p < 0.01)

The absence of significant differences in viability between TIMP-3 and GFP mRNA treatments at equal doses across all cell lines at 24 h likely reflects the time required for nanoparticle uptake and subsequent mRNA processing. The difference in sensitivity among cell lines suggests that TIMP-3, in addition to its established role in stabilizing

death receptors on the cell surface, may exert a cell type-specific regulatory effect on proliferative and survival pathways.

Several genes are differentially regulated in B16-F10 compared with B16-F1 cells [109], [110] In particular, B16-F10 cells express higher levels of tissue-type plasminogen activator (tPA) and its receptor LRP1, which correlate with enhanced ERK1/2 activation and MMP9 upregulation (Figure 34) [111]. Upon binding to LRP1, tPA activates the ERK1/2 cascade. Phosphorylated ERK1/2 then translocate into the nucleus, where it induces transcription factors such as Elk-1, c-Fos, and c-Myc. This, in turn, induces the expression of genes that promote cell cycle progression and survival, including cyclin D1 and Bcl-2 family members [112]. Moreover, ERK1/2 signaling enhances the expression of both tPA and MMP9, creating a positive feedback loop that sustains pathway activation and amplifies melanoma proliferation and invasion [111].

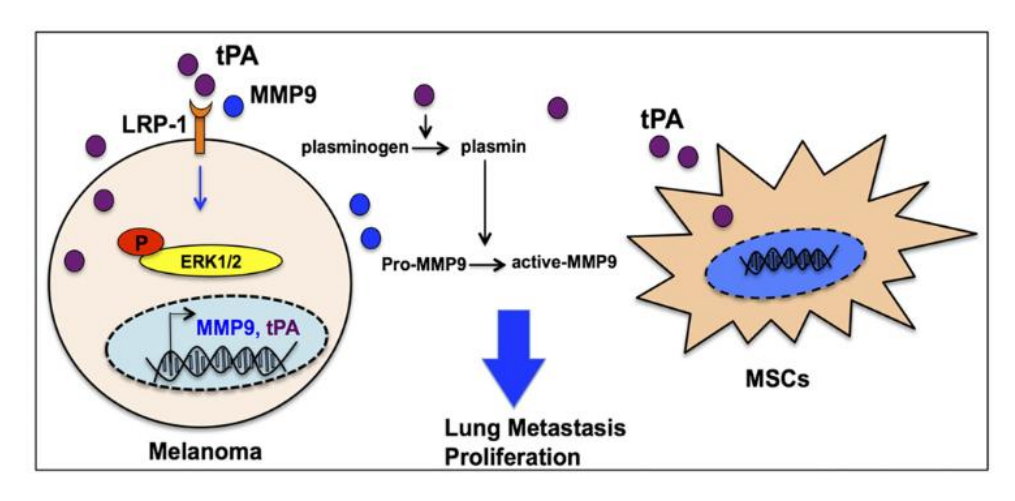


Figure 34: Effects of tPA and LRP1 on melanoma proliferation and metastasis

TIMP-3, which is also known to bind LRP1[113], [114], might competitively inhibit tPA binding, attenuating downstream ERK1/2 signaling, MMP9 expression, and consequently cell proliferation in B16-F10. In contrast, B16-F1, which have inherently lower levels of tPA and LRP1 expression, may rely less on this pathway and therefore show a weaker response to TIMP-3 treatment. Taken together, these considerations suggest that differential regulation of proliferative signaling could explain the distinct viability responses observed between B16-F10 and B16-F1 cells following TIMP-3 treatment.

Optimizing the experimental design by increasing the density of dose levels in the 1–6 μ g/mL range is expected to enhance the precision of dose–response modelling and IC₅₀ determination, while reducing the risk of missing concentration windows critical for revealing cell–specific TIMP–3 effects.

Hydrogel Biocompatibility Assay

Biocompatibility of the P407/P188 formulation was evaluated through indirect cytotoxicity testing of degradation supernatants. This approach mimics in vivo leachables and accounts for both polymer degradation products and secondary environmental changes, such as pH shifts. The tested poloxamer concentrations were derived from the hydrogel-to-medium ratios corresponding to the previously used mRNA doses (Table 3).

mRNA concentration (μg/ mL)	Poloxamer concentration (%)
0,01	0,018
0,06	0,108
0,1	0,18
0,6	1,08
1	1,8
6	10,8
10	18

Table 3: Poloxamer concentrations in degradation supernatants corresponding to the hydrogel-to-medium ratios corresponding to the previously tested mRNA doses

The dose-response curves obtained from the MTT assay (Figure 17) revealed a clear dose-dependent decrease in cell viability with increasing poloxamer concentrations. At the lowest concentrations (≤ 0.18 %), both B16-F1 and B16-F10 cell lines maintained viability levels above the 70% threshold defined for biocompatibility. At intermediate concentrations (1.08 and 1.8 %), different responses emerged between the two cell lines. B16 F1 exhibited an initial marked decrease in viability, followed by a robust recovery to nearly baseline levels at 72 h, whereas B16-F10 cells showed only a modest recovery ($\approx 66\%$), indicating a higher sensitivity to the degradation products. This differential response is likely attributable to intrinsic biological differences between the cell lines.

At the highest tested concentrations (10.8 % and 18 %), the hydrogel degradation products induced a strong and nearly complete loss of cell viability in both cell lines, with viability values dropping below 1% by 72 h. The reduced variability (SD) at these concentrations indicates that the cytotoxic effect was uniform across the cell population.

By contrast, Melan-A cells showed enhanced proliferation in the presence of degradation by-products compared with controls; however, at the highest concentration (10%) the effect reversed and became clearly cytotoxic, particularly at 72 h (Figure 36).

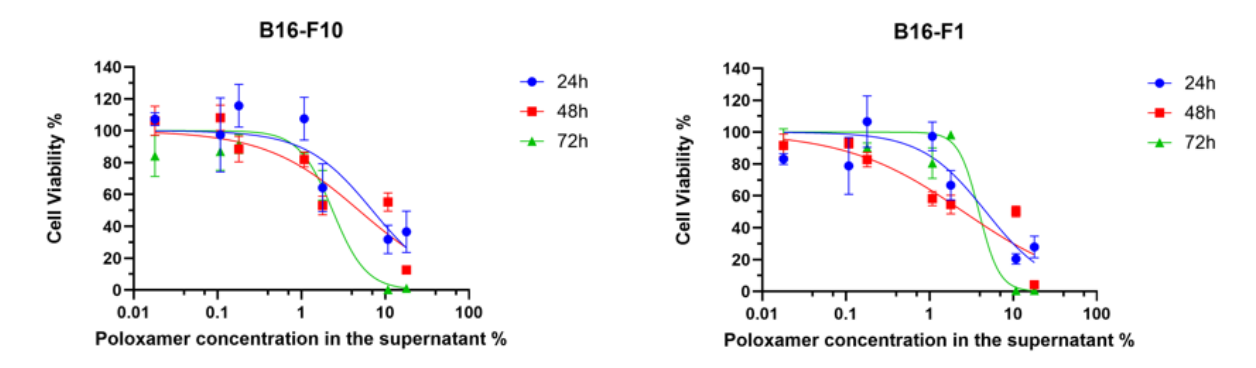


Figure 35: Dose-response curves of B16-F10 and B16-F1 cell viability following exposure to degradation supernatants of the P407/P188 hydrogel.

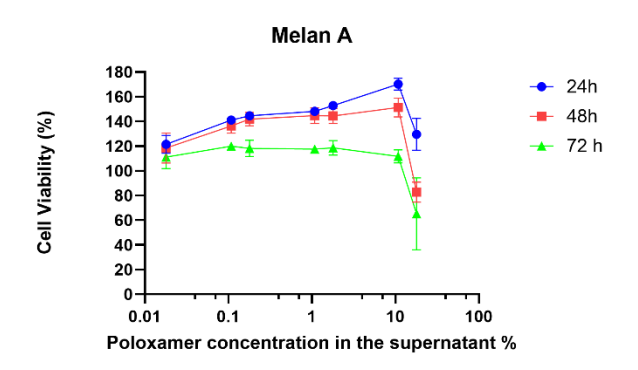


Figure 36: Viability of melan-a cells following exposure to degradation supernatants of the P407/P188 hydrogel

Consistent with in vitro evidence that Poloxamer 407 selectively induce cytotoxicity in cancer cells by fluidizing membranes, depleting intracellular ATP, and inhibiting drugefflux transporters[115], [116], [117], the divergent responses observed at intermediate doses likely reflect membrane-biophysical differences. The recovery observed in B16-F1 cells at suggests that, although degradation products impose an initial stress, cells can activate repair mechanisms and adapt if the exposure remains within tolerable limits. In contrast, B16-F10 cells may be more susceptible to surfactant-mediated membrane damage, potentially due to higher plasma membrane hydration and lower lipid order, which could facilitate partitioning of PPO blocks into the bilayer and amplify cytotoxic effects [118].

A significant contributing factor to the cytotoxicity observed at high concentration could be due to pH increase in the extracted medium after hydrogel incubation, as observed by Tuzkinka et al. in a similar experimental setup[119].

Importantly, understanding whether and how FBS interferes with the degradation of these hydrogels is essential for predicting in vivo performance.

5.5 In vitro efficacy analysis

ELISA

As a proof of concept, to further investigate the effect of TIMP-3 treatment on B16 F10 cells, MMP-9 levels were quantified by ELISA at 24 h and 72h under different experimental conditions (Figure 37). The quantification showed no reduction in the negative control, while both the positive control (TIMP-3 mRNA) and TIMP-3 NPs led to decreased MMP-9 expression. A marked reduction was also observed with hydrogel alone and with hydrogel-loaded TIMP-3 NPs, indicating cytotoxic effects attributable to the hydrogel.

ELISA for MMP-9 evaluation

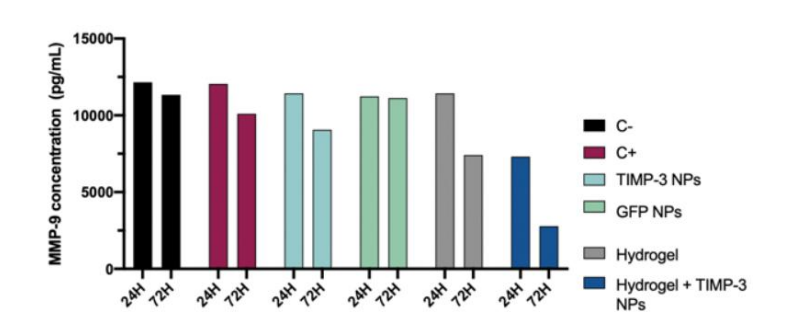


Figure 37: ELISA quantification of MMP-9 expression in B16 F10 cells

The signal generated in ELISA reflects the total pool of MMP-9 protein, regardless of whether it is in its active catalytic form, inactive proenzyme, or bound to TIMP-3.

Since this approach does not discriminate between these states, the observed reduction in MMP-9 levels in the positive control and following TIMP-3 treatment is consistent with the proposed TIMP-3/LRP-1 pathway. This finding suggests that TIMP-3 may inhibit melanoma invasion not only through its established role as a direct inhibitor of MMPs, but also by disrupting the ERK1/2-driven positive feedback associated with MMP9 overexpression.

In this experiment, a direct comparison between free NPs and hydrogel-loaded NPs was not feasible due to the observed cytotoxicity associated with the hydrogel formulation. It is important to note that this limitation does not stem from the material itself, as poloxamer is generally regarded as biocompatible and has been widely applied in local therapeutic delivery. Rather, the issue arises from the specific system design: with a formulation composed of 90% hydrogel and 10% (w/w) NPs, achieving higher mRNA doses necessarily required proportionally larger hydrogel volumes. At such volumes, cytotoxic effects became evident, as reflected by the decrease in MMP-9 expression

observed in hydrogel-only controls, likely due to a reduction in viability. Importantly, at 24 h the apparent difference between H and H+NPs is a normalization artifact—not a TIMP-3 effect—because ELISA values were normalized to total protein in the supernatant, which was approximately twofold higher in H+NPs than in H.

Western Blot

Intracellular TIMP-3 expression in B16-F10 and B16-F1 cells was assessed by Western blot. In the first attempts, no TIMP-3 signal was detected despite a robust housekeeping protein band (results not presented). Considering that the primary antibody used is validated for both human and mouse TIMP-3, it was hypothesized that the absence of detection may be attributable to suboptimal secondary antibody dilution rather than lack of target recognition. The secondary-antibody dilution was therefore increased from 1:5000 to 1:2500.

Despite this optimization, TIMP-3 was detected only in a subset of experimental conditions, specifically in B16-F1 cell lysates collected after 24 h of exposure and in B16-F10 cell lysates collected after 72 h. Western blot membranes are shown in Figure 18. Band intensities were quantified and normalized to β-actin to account for loading differences.

The ratios for hydrogel-containing conditions are reported for completeness but are not considered in the discussion, as no matching viability data are available and the reduced β -actin signal in these samples may reflect toxicity-induced decreases in β -actin, thereby biasing normalization. TIMP-3/ β -actin ratios indicated that in B16-F1 (24 h) TIMP-3 levels in TIMP-3 NPs-treated samples were slightly lower than the control (\approx 0.8), whereas in B16-F10 (72 h) both nanoparticle treatments were markedly lower than the corresponding control (\approx 0.35 for GFP NPs; \approx 0.30 for TIMP-3 NPs). All ratios should nevertheless be interpreted with caution, as treatment-dependent effects on cell viability can bias β -actin-based normalization.

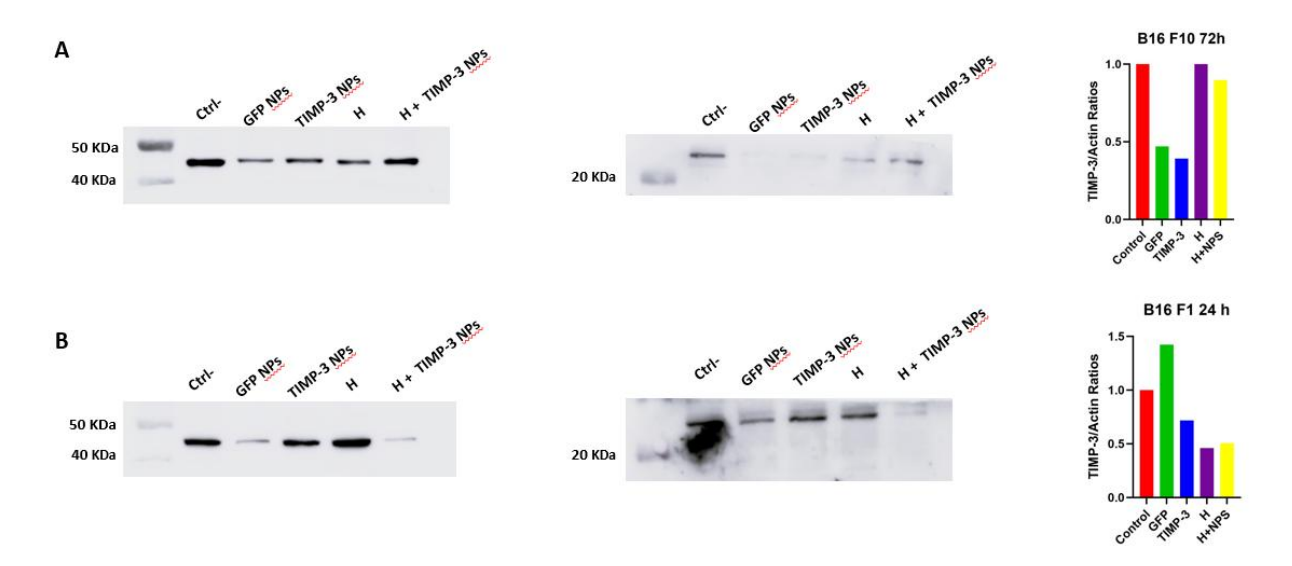


Figure 38: Western blot analysis of TIMP-3 expression in B16F10 (A) and B16F1 (B) cells following 24 h and 72 h incubation under different treatment conditions. Representative blots show TIMP-3 (left panels) and β -actin (loading control, right panels). Quantification of TIMP-3/actin ratios is reported in the graphs (right). Experimental conditions: control (Ctrl-), GFP mRNA nanoparticles (GFP NPs), TIMP-3 mRNA nanoparticles (TIMP-3 NPs), hydrogel alone (H), and hydrogel-loaded TIMP-3 nanoparticles (H + TIMP-3 NPs).

In B16-F1 cells at 24 h, two distinct bands were visible: a lighter band, corresponding to the unglycosylated form, and a heavier band, corresponding to the glycosylated form, with the unglycosylated form being more pronounced across all conditions. In B16-F10 cells at 72 h, a TIMP-3 band was detected, although it was difficult to determine with certainty whether the signal corresponded to two distinct isoforms or was influenced by background noise.

Given that TIMP-3 is a secreted protein with strong affinity for the extracellular matrix, analysis of cell lysates alone does not accurately capture its expression profile. Complementary assessment of the conditioned medium and an ECM-bound fraction—recovered by disrupting protein–glycosaminoglycan interactions—would provide a more complete picture of TIMP-3 dynamics.

While intracellular measurements are inherently partial, these results suggest that the underexpression of endogenous TIMP-3 in melanoma cell lines is not attributable to transcriptional inefficiencies, as intracellular protein was detected, but may rather be linked to post-translational mechanisms causing intracellular retention. In B16-F1 cells, the predominance of the unglycosylated form at 24 h indicates that incomplete glycosylation could play a role in this retention. Unfortunately, the absence of detectable bands at 72 h precludes further clarification. It would have been particularly informative to establish whether the prevalence of the unglycosylated form persisted over time: in the control condition, this could have clarified whether the underexpression of TIMP-3 in metastatic melanoma is associated with an immature glycosylation state; in the treatment condition, where TIMP-3 overexpression is induced, persistence of the

unglycosilated form could also provide an explanation for the reduced efficacy of TIMP-3 in this cell line. In B16-F10, the low intracellular accumulation at 72 h may reflect a combination of enhanced exocytosis and treatment-related reductions in viability.

Additional step in the protocol optimization for intracellular TIMP-3 detection should include verification of lysis efficiency and extraction completeness; systematic titration of primary and secondary antibodies to maximize specific signal while minimizing background; and adoption of total-protein normalization (stain-free imaging or Ponceau S) in conjunction with housekeeping controls. In addition, full, uncropped membranes should be examined to detect potential higher-molecular-weight species indicative of multimerization or abnormal processing, and enzymatic deglycosylation (e.g., PNGase F, Endo H) should be performed to confirm glycosylation heterogeneity.

5.6 Further characterisation

A therapeutic window in which the KH polymer–associated cytotoxicity was limited, and TIMP-3 cargo activity remained evident was established. Selective efficacy of the treatment was demonstrated: TIMP-3 overexpression reduced viability in B16-F10, with no comparable effect in B16-F1 or Melan-a. This selectivity is consistent with engagement of the tPA-LRP1/ERK1/2/MMP-9 axis, as indicated by decreased extracellular MMP-9 on ELISA.

While the P407/P188 hydrogel formulation met the requirements for injectability, the evaluation of the complete system was limited by design-related issues. Completing the formulation by manual pipetting resulted in incomplete mixing, which altered local poloxamer and PBS concentrations, compromising gelation reproducibility. A 96-well Transwell setup was considered to directly assess hydrogel cytotoxicity and test the loaded system. However, the receiver (bottom) plate was not tissue-culture treated and did not support cell adhesion despite coating attempts. In the absence of matched viability data, the WB and ELISA results for the hydrogel-containing conditions cannot be interpreted reliably. Future experiments should include parallel viability measurements at the same time points to contextualize these data. As an additional control, steam sterilization by autoclaving of the hydrogel formulation should be evaluated to confirm that the observed toxicity arises from the high hydrogel to medium ratio in the in vitro setup rather than from contamination.

Beyond the optimizations already proposed for the individual assays and their extension to all cell lines where not yet done, further characterization could help clarify the specific role of TIMP-3 in metastatic melanoma progression. Migration and apoptosis assays should determine whether B16-F10 cells exhibit greater inhibition of motility and increased apoptotic susceptibility than B16-F1. It should also be noted that, while TIMP-3 binding to LRP1 is desirable because it antagonizes the tPA-LRP1 axis, it also promotes endocytic uptake, thereby reducing extracellular availability, potentially attenuating

MMP-inhibitory activity, and influencing death receptor-mediated apoptosis. Secretome analysis should be used to determine a temporal profile of TIMP-3 secretion, assess the kinetics of TIMP-3/LRP1 interaction and evaluate the resultant changes in extracellular protein composition and associated molecular pathways.

5.7 Conclusion

Melanoma progression and metastasis are driven by complex alterations in gene regulation that govern cell proliferation, invasion, and survival. Extensive experimental evidence reveals that melanoma cells can adopt different signaling paradigms depending on their molecular expression profile. The present findings highlight that differential gene regulation provides a rationale for therapeutic strategies that selectively target the more aggressive melanoma phenotype. By antagonizing tPA-mediated LRPI activation, TIMP-3 may attenuate malignant signaling in pathway-dependent tumors, and microenvironmental antiangiogenic effects could further amplify this response. Accordingly, evaluation in in vivo models that recapitulate tumor-host interactions is warranted, where efficacy may translate into more pronounced tumor regression than observed in simplified in vitro systems. In parallel, improved implementation of the hydrogel formulation could enable localized, sustained intratumoral delivery of TIMP-3, thereby enhancing the therapeutic index in pathway-dependent tumors.

Bibliography

- [1] S. Carr, C. Smith, and J. Wernberg, 'Epidemiology and Risk Factors of Melanoma', Surg. Clin. North Am., vol. 100, no. 1, pp. 1–12, Feb. 2020, doi: 10.1016/j.suc.2019.09.005.
- [2] W. W. Dzwierzynski, 'Melanoma Risk Factors and Prevention', *Clin. Plast. Surg.*, vol. 48, no. 4, pp. 543–550, Oct. 2021, doi: 10.1016/j.cps.2021.05.001.
- [3] S. Carr, C. Smith, and J. Wernberg, 'Epidemiology and Risk Factors of Melanoma', Surg. Clin. North Am., vol. 100, no. 1, pp. 1–12, Feb. 2020, doi: 10.1016/j.suc.2019.09.005.
- [4] R. Laskar *et al.*, 'Risk factors for melanoma by anatomical site: an evaluation of aetiological heterogeneity*', *Br. J. Dermatol.*, vol. 184, no. 6, pp. 1085–1093, June 2021, doi: 10.1111/bjd.19705.
- [5] S. Carr, C. Smith, and J. Wernberg, 'Epidemiology and Risk Factors of Melanoma', Surg. Clin. North Am., vol. 100, no. 1, pp. 1–12, Feb. 2020, doi: 10.1016/j.suc.2019.09.005.
- [6] E. Z. Keung and J. E. Gershenwald, 'The eighth edition American Joint Committee on Cancer (AJCC) melanoma staging system: implications for melanoma treatment and care', *Expert Rev. Anticancer Ther.*, vol. 18, no. 8, pp. 775–784, Aug. 2018, doi: 10.1080/14737140.2018.1489246.
- [7] R. I. Hartman and J. Y. Lin, 'Cutaneous Melanoma—A Review in Detection, Staging, and Management', *Hematol. Oncol. Clin. North Am.*, vol. 33, no. 1, pp. 25–38, Feb. 2019, doi: 10.1016/j.hoc.2018.09.005.
- [8] G. V. Long, S. M. Swetter, A. M. Menzies, J. E. Gershenwald, and R. A. Scolyer, 'Cutaneous melanoma', *The Lancet*, vol. 402, no. 10400, pp. 485–502, Aug. 2023, doi: 10.1016/s0140-6736(23)00821-8.
- [9] K. Nguyen, E. Hignett, and A. Khachemoune, 'Current and emerging treatment options for metastatic melanoma: a focused review', *Dermatol. Online J.*, vol. 26, no. 7, 2020, doi: 10.5070/D3267049551.
- [10] R. W. Jenkins and D. E. Fisher, 'Treatment of Advanced Melanoma in 2020 and Beyond', *J. Invest. Dermatol.*, vol. 141, no. 1, pp. 23–31, Jan. 2021, doi: 10.1016/j.jid.2020.03.943.
- [11] A. Fateeva, K. Eddy, and S. Chen, 'Current State of Melanoma Therapy and Next Steps: Battling Therapeutic Resistance', *Cancers*, vol. 16, no. 8, p. 1571, Jan. 2024, doi: 10.3390/cancers16081571.

- [12] S. S. Moni *et al.*, 'Advances in Materials Science for Precision Melanoma Therapy: Nanotechnology-Enhanced Drug Delivery Systems', *Pharmaceutics*, vol. 17, no. 3, p. 296, Mar. 2025, doi: 10.3390/pharmaceutics17030296.
- [13] H. Mishra, P. K. Mishra, A. Ekielski, M. Jaggi, Z. Iqbal, and S. Talegaonkar, 'Melanoma treatment: from conventional to nanotechnology', *J. Cancer Res. Clin. Oncol.*, vol. 144, no. 12, pp. 2283–2302, Dec. 2018, doi: 10.1007/s00432-018-2726-1.
- [14] E. Blanco, H. Shen, and M. Ferrari, 'Principles of nanoparticle design for overcoming biological barriers to drug delivery', *Nat. Biotechnol.*, vol. 33, no. 9, pp. 941–951, Sept. 2015, doi: 10.1038/nbt.3330.
- [15] 'Delivering nanomedicine to solid tumors | Nature Reviews Clinical Oncology'. Accessed: Oct. 10, 2025. [Online]. Available: https://www.nature.com/articles/nrclinonc.2010.139
- [16] J. P. M. Almeida, A. L. Chen, A. Foster, and R. Drezek, 'In vivo biodistribution of nanoparticles', *Nanomed.*, vol. 6, no. 5, pp. 815–835, July 2011, doi: 10.2217/nnm.11.79.
- [17] Y. Hui *et al.*, 'Role of Nanoparticle Mechanical Properties in Cancer Drug Delivery', *ACS Nano*, vol. 13, no. 7, pp. 7410–7424, July 2019, doi: 10.1021/acsnano.9b03924.
- [18] A. M. Wokovich, S. Prodduturi, W. H. Doub, A. S. Hussain, and L. F. Buhse, 'Transdermal drug delivery system (TDDS) adhesion as a critical safety, efficacy and quality attribute', *Eur. J. Pharm. Biopharm. Off. J. Arbeitsgemeinschaft Pharm. Verfahrenstechnik EV*, vol. 64, no. 1, pp. 1–8, Aug. 2006, doi: 10.1016/j.ejpb.2006.03.009.
- [19] M. Navalón-López, A. Dols-Perez, S. Grijalvo, C. Fornaguera, and S. Borrós, 'Unravelling the role of individual components in pBAE/polynucleotide polyplexes in the synthesis of tailored carriers for specific applications: on the road to rational formulations', *Nanoscale Adv.*, vol. 5, no. 6, pp. 1611–1623, doi: 10.1039/d2na00800a.
- [20] J. S. Lee and J. Feijen, 'Polymersomes for drug delivery: Design, formation and characterization', *J. Controlled Release*, vol. 161, no. 2, pp. 473–483, July 2012, doi: 10.1016/j.jconrel.2011.10.005.
- [21] A.-M. Caminade and C.-O. Turrin, 'Dendrimers for drug delivery', *J. Mater. Chem. B*, vol. 2, no. 26, pp. 4055–4066, June 2014, doi: 10.1039/C4TB00171K.
- [22] Y. Yue and C. Wu, 'Progress and perspectives in developing polymeric vectors for in vitro gene delivery', *Biomater. Sci.*, vol. 1, no. 2, pp. 152–170, Jan. 2013, doi: 10.1039/C2BM00030J.

- [23] A. Kumari, S. K. Yadav, and S. C. Yadav, 'Biodegradable polymeric nanoparticles based drug delivery systems', *Colloids Surf. B Biointerfaces*, vol. 75, no. 1, pp. 1–18, Jan. 2010, doi: 10.1016/j.colsurfb.2009.09.001.
- [24] G. Mahmoodi Chalbatani *et al.*, 'Small interfering RNAs (siRNAs) in cancer therapy: a nano-based approach', *Int. J. Nanomedicine*, vol. 14, pp. 3111–3128, 2019, doi: 10.2147/IJN.S200253.
- [25] H. Lv, S. Zhang, B. Wang, S. Cui, and J. Yan, 'Toxicity of cationic lipids and cationic polymers in gene delivery', *J. Control. Release Off. J. Control. Release Soc.*, vol. 114, no. 1, pp. 100–109, Aug. 2006, doi: 10.1016/j.jconrel.2006.04.014.
- [26] E. U. Okon, G. Hammed, P. Abu El Wafa, O. Abraham, N. Case, and E. Henry, 'In-vitro cytotoxicity of Polyethyleneimine on HeLa and Vero Cells', *Int. J. Innov. Appl. Stud.*, vol. 5, no. 3, pp. 192–199, Mar. 2014.
- [27] D. M. Lynn and R. Langer, 'Degradable Poly(β-amino esters): Synthesis, Characterization, and Self-Assembly with Plasmid DNA', *J. Am. Chem. Soc.*, vol. 122, no. 44, pp. 10761–10768, Nov. 2000, doi: 10.1021/ja0015388.
- [28] J. Zhang *et al.*, 'Poly(β-amino ester)s-based nanovehicles: Structural regulation and gene delivery', *Mol. Ther. Nucleic Acids*, vol. 32, pp. 568–581, June 2023, doi: 10.1016/j.omtn.2023.04.019.
- [29] C. Fornaguera, C. Castells-Sala, M. A. Lázaro, A. Cascante, and S. Borrós, 'Development of an optimized freeze-drying protocol for OM-PBAE nucleic acid polyplexes', *Int. J. Pharm.*, vol. 569, p. 118612, Oct. 2019, doi: 10.1016/j.ijpharm.2019.118612.
- [30] J. R. Magaña Rodriguez, M. Guerra-Rebollo, S. Borrós, and C. Fornaguera, 'Nucleic acid-loaded poly(beta-aminoester) nanoparticles for cancer nano-immuno therapeutics: the good, the bad, and the future', *Drug Deliv. Transl. Res.*, vol. 14, no. 12, pp. 3477–3493, Dec. 2024, doi: 10.1007/s13346-024-01585-y.
- [31] N. Segovia, P. Dosta, A. Cascante, V. Ramos, and S. Borrós, 'Oligopeptide-terminated poly(β-amino ester)s for highly efficient gene delivery and intracellular localization', *Acta Biomater.*, vol. 10, no. 5, pp. 2147–2158, May 2014, doi: 10.1016/j.actbio.2013.12.054.
- [32] P. Dosta, N. Segovia, A. Cascante, V. Ramos, and S. Borrós, 'Surface charge tunability as a powerful strategy to control electrostatic interaction for high efficiency silencing, using tailored oligopeptide-modified poly(beta-amino ester)s (PBAEs)', *Acta Biomater.*, vol. 20, pp. 82–93, July 2015, doi: 10.1016/j.actbio.2015.03.029.

- [33] C. Fornaguera *et al.*, 'mRNA Delivery System for Targeting Antigen-Presenting Cells In Vivo', *Adv. Healthc. Mater.*, vol. 7, no. 17, p. e1800335, Sept. 2018, doi: 10.1002/adhm.201800335.
- [34] P. Dosta, V. Ramos, and S. Borrós, 'Stable and efficient generation of poly(β-amino ester)s for RNAi delivery', *Mol. Syst. Des. Eng.*, vol. 3, no. 4, pp. 677–689, Aug. 2018, doi: 10.1039/C8ME00006A.
- [35] M. Ramamoorth and A. Narvekar, 'Non viral vectors in gene therapy- an overview', *J. Clin. Diagn. Res. JCDR*, vol. 9, no. 1, pp. GE01-06, Jan. 2015, doi: 10.7860/JCDR/2015/10443.5394.
- [36] K. R. Rhodes *et al.*, 'Biodegradable Cationic Polymer Blends for Fabrication of Enhanced Artificial Antigen Presenting Cells to Treat Melanoma', *ACS Appl. Mater. Interfaces*, vol. 13, no. 7, pp. 7913–7923, Feb. 2021, doi: 10.1021/acsami.0c19955.
- [37] S. Y. Tzeng, K. K. Patel, D. R. Wilson, R. A. Meyer, K. R. Rhodes, and J. J. Green, 'In situ genetic engineering of tumors for long-lasting and systemic immunotherapy', *Proc. Natl. Acad. Sci.*, vol. 117, no. 8, pp. 4043–4052, Feb. 2020, doi: 10.1073/pnas.1916039117.
- [38] Z. Chu *et al.*, 'Enhanced gene transfection and induction of apoptosis in melanoma cells by branched poly(β-amino ester)s with uniformly distributed branching units', *J. Controlled Release*, vol. 367, pp. 197–208, Mar. 2024, doi: 10.1016/j.jconrel.2024.01.026.
- [39] J. Mahin, X. Xu, L. Li, and C. Zhang, 'cGAS/STING in skin melanoma: from molecular mechanisms to therapeutics', *Cell Commun. Signal.*, vol. 22, no. 1, p. 553, Nov. 2024, doi: 10.1186/s12964-024-01860-y.
- [40] E. Ben-Akiva *et al.*, 'Biodegradable lipophilic polymeric mRNA nanoparticles for ligand-free targeting of splenic dendritic cells for cancer vaccination', *Proc. Natl. Acad. Sci.*, vol. 120, no. 26, p. e2301606120, June 2023, doi: 10.1073/pnas.2301606120.
- [41] A. S. Priya *et al.*, 'Comprehensive Review of Hydrogel Synthesis, Characterization, and Emerging Applications', *J. Compos. Sci.*, vol. 8, no. 11, p. 457, Nov. 2024, doi: 10.3390/jcs8110457.
- [42] T.-C. Ho *et al.*, 'Hydrogels: Properties and Applications in Biomedicine', *Molecules*, vol. 27, no. 9, p. 2902, Jan. 2022, doi: 10.3390/molecules27092902.
- [43] S. H. Aswathy, U. Narendrakumar, and I. Manjubala, 'Commercial hydrogels for biomedical applications', *Heliyon*, vol. 6, no. 4, Apr. 2020, doi: 10.1016/j.heliyon.2020.e03719.

- [44] J. R. Choi, K. W. Yong, J. Y. Choi, and A. C. Cowie, 'Recent Advances in Photo-Crosslinkable Hydrogels for Biomedical Applications', *BioTechniques*, vol. 66, no. 1, pp. 40–53, Jan. 2019, doi: 10.2144/btn-2018-0083.
- [45] S. Chatterjee and P. C. Hui, 'Review of Applications and Future Prospects of Stimuli-Responsive Hydrogel Based on Thermo-Responsive Biopolymers in Drug Delivery Systems', *Polymers*, vol. 13, no. 13, p. 2086, Jan. 2021, doi: 10.3390/polym13132086.
- [46] R. Fan *et al.*, 'Thermosensitive Hydrogels and Advances in Their Application in Disease Therapy', *Polymers*, vol. 14, no. 12, p. 2379, Jan. 2022, doi: 10.3390/polym14122379.
- [47] S. Pardeshi *et al.*, 'Functional Thermoresponsive Hydrogel Molecule to Material Design for Biomedical Applications', *Polymers*, vol. 14, no. 15, p. 3126, Jan. 2022, doi: 10.3390/polym14153126.
- [48] L. Bonetti, L. De Nardo, and S. Farè, 'Thermo-Responsive Methylcellulose Hydrogels: From Design to Applications as Smart Biomaterials', *Tissue Eng. Part B Rev.*, vol. 27, no. 5, pp. 486–513, Oct. 2021, doi: 10.1089/ten.teb.2020.0202.
- [49] A. M. Bodratti and P. Alexandridis, 'Amphiphilic block copolymers in drug delivery: advances in formulation structure and performance', *Expert Opin. Drug Deliv.*, vol. 15, no. 11, pp. 1085–1104, Nov. 2018, doi: 10.1080/17425247.2018.1529756.
- [50] A. M. Bodratti and P. Alexandridis, 'Formulation of Poloxamers for Drug Delivery', *J. Funct. Biomater.*, vol. 9, no. 1, p. 11, Mar. 2018, doi: 10.3390/jfb9010011.
- [51] 'Investigation and Characterization of Factors Affecting Rheological Properties of Poloxamer-Based Thermo-Sensitive Hydrogel'. Accessed: Oct. 10, 2025. [Online]. Available: https://www.mdpi.com/2073-4360/14/24/5353
- [52] H. Abdeltawab, D. Svirskis, and M. Sharma, 'Formulation strategies to modulate drug release from poloxamer based in situ gelling systems', *Expert Opin. Drug Deliv.*, vol. 17, no. 4, pp. 495–509, Apr. 2020, doi: 10.1080/17425247.2020.1731469.
- [53] E. Brambilla *et al.*, 'Poloxamer-Based Hydrogel as Drug Delivery System: How Polymeric Excipients Influence the Chemical-Physical Properties', *Polymers*, vol. 14, no. 17, p. 3624, Jan. 2022, doi: 10.3390/polym14173624.
- [54] E. Giuliano, D. Paolino, M. Fresta, and D. Cosco, 'Mucosal Applications of Poloxamer 407-Based Hydrogels: An Overview', *Pharmaceutics*, vol. 10, no. 3, p. 159, Sept. 2018, doi: 10.3390/pharmaceutics10030159.
- [55] K. A. Soliman, K. Ullah, A. Shah, D. S. Jones, and T. R. R. Singh, 'Poloxamer-based *in situ* gelling thermoresponsive systems for ocular drug delivery applications', *Drug Discov. Today*, vol. 24, no. 8, pp. 1575–1586, Aug. 2019, doi: 10.1016/j.drudis.2019.05.036.

- [56] E. Brambilla *et al.*, 'Poloxamer-Based Hydrogel as Drug Delivery System: How Polymeric Excipients Influence the Chemical-Physical Properties', *Polymers*, vol. 14, no. 17, p. 3624, Jan. 2022, doi: 10.3390/polym14173624.
- [57] F. Zhang, 'Fluorouracil Treatment Via Colon for Colorectal Cancer: an Exploratory Study', clinicaltrials.gov, Clinical trial registration NCT06385418, June 2024. Accessed: Oct. 10, 2025. [Online]. Available: https://clinicaltrials.gov/study/NCT06385418
- [58] 'Phenotype Switching and the Melanoma Microenvironment; Impact on Immunotherapy and Drug Resistance'. Accessed: Oct. 10, 2025. [Online]. Available: https://www.mdpi.com/1422-0067/24/2/1601
- [59] S. Subhadarshini, S. Sahoo, S. Debnath, J. A. Somarelli, and M. K. Jolly, 'Dynamical modelling of proliferative-invasive plasticity and IFN_Y signaling in melanoma reveals mechanisms of PD-L1 expression heterogeneity', June 12, 2023, *bioRxiv*. doi: 10.1101/2023.01.09.523355.
- [60] O. Szczygielski, E. Dąbrowska, S. Niemyjska, A. Przylipiak, and M. Zajkowska, 'Targeting Matrix Metalloproteinases and Their Inhibitors in Melanoma', *Int. J. Mol. Sci.*, vol. 25, no. 24, p. 13558, Jan. 2024, doi: 10.3390/ijms252413558.
- [61] A. Bastian, L. Nichita, and S. Zurac, 'Matrix metalloproteinases in melanoma with and without regression', in *The role of matrix metalloproteinase in human body pathologies*, F. Travascio, Ed., London: IntechOpen, 2017. doi: 10.5772/intechopen.72931.
- [62] A. M. Das *et al.*, 'Tissue inhibitor of metalloproteinase-3 (TIMP3) expression decreases during melanoma progression and inhibits melanoma cell migration', *Eur. J. Cancer*, vol. 66, pp. 34–46, Oct. 2016, doi: 10.1016/j.ejca.2016.06.020.
- [63] G. A. Cabral-Pacheco *et al.*, 'The Roles of Matrix Metalloproteinases and Their Inhibitors in Human Diseases', *Int. J. Mol. Sci.*, vol. 21, no. 24, p. 9739, Dec. 2020, doi: 10.3390/ijms21249739.
- [64] C. Figueiredo and A. C. Araujo e Silva, 'Role of Metalloproteinases in Melanoma Growth and Progression', in *Proteases in Human Diseases*, S. Chakraborti, T. Chakraborti, and N. S. Dhalla, Eds, Singapore: Springer, 2017, pp. 91–102. doi: 10.1007/978-981-10-3162-5_5.
- [65] A. Rotte, M. Martinka, and G. Li, 'MMP2 expression is a prognostic marker for primary melanoma patients', *Cell. Oncol. Dordr. Neth.*, vol. 35, no. 3, pp. 207–216, June 2012, doi: 10.1007/s13402-012-0080-x.
- [66] A. Desch *et al.*, 'Highly Invasive Melanoma Cells Activate the Vascular Endothelium via an MMP-2/Integrin ανβ5–Induced Secretion of VEGF-A', *Am. J. Pathol.*, vol. 181, no. 2, pp. 693–705, Aug. 2012, doi: 10.1016/j.ajpath.2012.04.012.

- [67] S. Niland and J. A. Eble, 'Hold on or Cut? Integrin- and MMP-Mediated Cell-Matrix Interactions in the Tumor Microenvironment', *Int. J. Mol. Sci.*, vol. 22, no. 1, p. 238, Dec. 2020, doi: 10.3390/ijms22010238.
- [68] B. S. Mastalier Manolescu *et al.*, 'MMP1, MMP9, MMP11 and MMP13 in melanoma and its metastasis key points in understanding the mechanisms and celerity of tumor dissemination', *Romanian J. Morphol. Embryol. Rev. Roum. Morphol. Embryol.*, vol. 65, no. 1, pp. 45–52, 2024, doi: 10.47162/RJME.65.1.06.
- [69] T. Maretzky *et al.*, 'ADAM10 mediates E-cadherin shedding and regulates epithelial cell-cell adhesion, migration, and beta-catenin translocation', *Proc. Natl. Acad. Sci. U. S. A.*, vol. 102, no. 26, pp. 9182–9187, June 2005, doi: 10.1073/pnas.0500918102.
- [70] H. Kataoka, 'EGFR ligands and their signaling scissors, ADAMs, as new molecular targets for anticancer treatments', *J. Dermatol. Sci.*, vol. 56, no. 3, pp. 148–153, Dec. 2009, doi: 10.1016/j.jdermsci.2009.10.002.
- [71] G. Murphy, 'The ADAMs: signalling scissors in the tumour microenvironment', *Nat. Rev. Cancer*, vol. 8, no. 12, pp. 929–941, Dec. 2008, doi: 10.1038/nrc2459.
- [72] M. Schulte *et al.*, 'ADAM10 regulates FasL cell surface expression and modulates FasL-induced cytotoxicity and activation-induced cell death', *Cell Death Differ.*, vol. 14, no. 5, pp. 1040–1049, May 2007, doi: 10.1038/sj.cdd.4402101.
- [73] S. Kumar, N. Rao, and R. Ge, 'Emerging Roles of ADAMTSs in Angiogenesis and Cancer', *Cancers*, vol. 4, no. 4, pp. 1252–1299, Dec. 2012, doi: 10.3390/cancers4041252.
- [74] X. Wei *et al.*, 'Mutational and Functional Analysis Reveals ADAMTS18 Metalloproteinase as a Novel Driver in Melanoma', *Mol. Cancer Res.*, vol. 8, no. 11, pp. 1513–1525, Nov. 2010, doi: 10.1158/1541-7786.MCR-10-0262.
- [75] S. Kumar, N. Rao, and R. Ge, 'Emerging Roles of ADAMTSs in Angiogenesis and Cancer', *Cancers*, vol. 4, no. 4, pp. 1252–1299, Dec. 2012, doi: 10.3390/cancers4041252.
- [76] N. Rao *et al.*, 'ADAMTS4 and its proteolytic fragments differentially affect melanoma growth and angiogenesis in mice', *Int. J. Cancer*, vol. 133, no. 2, pp. 294–306, 2013, doi: 10.1002/ijc.28037.
- [77] S. Cal and C. López-Otín, 'ADAMTS proteases and cancer', *Matrix Biol.*, vol. 44–46, pp. 77–85, May 2015, doi: 10.1016/j.matbio.2015.01.013.
- [78] W.-H. Yu, S. C. Yu, Q. Meng, K. Brew, and J. F. Woessner, 'TIMP-3 Binds to Sulfated Glycosaminoglycans of the Extracellular Matrix *', *J. Biol. Chem.*, vol. 275, no. 40, pp. 31226–31232, Oct. 2000, doi: 10.1074/jbc.M000907200.

- [79] J. Verstappen and J. W. Von den Hoff, 'Tissue inhibitors of metalloproteinases (TIMPs): their biological functions and involvement in oral disease', *J. Dent. Res.*, vol. 85, no. 12, pp. 1074–1084, Dec. 2006, doi: 10.1177/154405910608501202.
- [80] J. H. J. Betts, 'Molecular mechanisms of TIMP-3 turnover in Sorsby Fundus Dystrophy', doctoral, University of East Anglia, 2024. Accessed: Oct. 07, 2025. [Online]. Available: https://ueaeprints.uea.ac.uk/id/eprint/96214/
- [81] C. Doherty, 'Design of a TIMP-3 mutant with an increased half-life for improved protection against cartilage breakdown', http://purl.org/dc/dcmitype/Text, University of Oxford, 2015. Accessed: Oct. 07, 2025. [Online]. Available: https://ora.ox.ac.uk/objects/uuid:0f7c6627-4732-402f-920a-576fa6ad7400
- [82] K.-H. Kang, S.-Y. Park, S. B. Rho, and J.-H. Lee, 'Tissue inhibitor of metalloproteinases-3 interacts with angiotensin II type 2 receptor and additively inhibits angiogenesis', *Cardiovasc. Res.*, vol. 79, no. 1, pp. 150–160, July 2008, doi: 10.1093/cvr/cvn072.
- [83] J. H. Qi *et al.*, 'A novel function for tissue inhibitor of metalloproteinases-3 (TIMP3): inhibition of angiogenesis by blockage of VEGF binding to VEGF receptor-2', *Nat. Med.*, vol. 9, no. 4, pp. 407–415, Apr. 2003, doi: 10.1038/nm846.
- [84] M. L. M. Lamfers *et al.*, 'Tissue Inhibitor of Metalloproteinase-3 Expression from an Oncolytic Adenovirus Inhibits Matrix Metalloproteinase Activity In vivo without Affecting Antitumor Efficacy in Malignant Glioma', *Cancer Res.*, vol. 65, no. 20, pp. 9398–9405, Oct. 2005, doi: 10.1158/0008-5472.CAN-04-4264.
- [85] A. H. Baker, S. J. George, A. B. Zaltsman, G. Murphy, and A. C. Newby, 'Inhibition of invasion and induction of apoptotic cell death of cancer cell lines by overexpression of TIMP-3', *Br. J. Cancer*, vol. 79, no. 9, pp. 1347–1355, Mar. 1999, doi: 10.1038/sj.bjc.6690217.
- [86] M. Ahonen *et al.*, 'Antitumor Activity and Bystander Effect of Adenovirally Delivered Tissue Inhibitor of Metalloproteinases-3', *Mol. Ther.*, vol. 5, no. 6, pp. 705–715, June 2002, doi: 10.1006/mthe.2002.0606.
- [87] M. A. Majid, V. A. Smith, D. L. Easty, A. H. Baker, and A. C. Newby, 'Adenovirus mediated gene delivery of tissue inhibitor of metalloproteinases-3 induces death in retinal pigment epithelial cells', *Br. J. Ophthalmol.*, vol. 86, no. 1, pp. 97–101, Jan. 2002, doi: 10.1136/bjo.86.1.97.
- [88] M. Ahonen, A. H. Baker, and V. M. Kähäri, 'Adenovirus-mediated gene delivery of tissue inhibitor of metalloproteinases-3 inhibits invasion and induces apoptosis in melanoma cells', *Cancer Res.*, vol. 58, no. 11, pp. 2310–2315, June 1998.

- [89] M. Ahonen *et al.*, 'Tissue inhibitor of metalloproteinases–3 induces apoptosis in melanoma cells by stabilization of death receptors', *Oncogene*, vol. 22, no. 14, pp. 2121–2134, Apr. 2003, doi: 10.1038/sj.onc.1206292.
- [90] P. Dosta, V. Ramos, and S. Borrós, 'Stable and efficient generation of poly(β-amino ester)s for RNAi delivery', *Mol. Syst. Des. Eng.*, vol. 3, no. 4, pp. 677–689, Aug. 2018, doi: 10.1039/C8ME00006A.
- [91] M. Navalón-López, A. Dols-Perez, S. Grijalvo, C. Fornaguera, and S. Borrós, 'Unravelling the role of individual components in pBAE/polynucleotide polyplexes in the synthesis of tailored carriers for specific applications: on the road to rational formulations', *Nanoscale Adv.*, vol. 5, no. 6, pp. 1611–1623, Mar. 2023, doi: 10.1039/D2NA00800A.
- [92] C. Bofill Bonet, 'Design of a local delivery system for the treatment of abdominal aortic aneurysm', Ph.D. Thesis, Universitat Ramon Llull, 2024. Accessed: Aug. 07, 2025. [Online]. Available: https://www.tdx.cat/handle/10803/691471
- [93] H. T. Nia, L. L. Munn, and R. K. Jain, 'Physical traits of cancer', *Science*, vol. 370, no. 6516, p. eaaz0868, Oct. 2020, doi: 10.1126/science.aaz0868.
- [94] A. C. Marques, P. C. Costa, S. Velho, and M. H. Amaral, 'Rheological and Injectability Evaluation of Sterilized Poloxamer-407-Based Hydrogels Containing Docetaxel-Loaded Lipid Nanoparticles', *Gels Basel Switz.*, vol. 10, no. 5, p. 307, May 2024, doi: 10.3390/gels10050307.
- [95] J. Burak, K. P. Grela, J. Pluta, B. Karolewicz, and D. M. Marciniak, 'Impact of sterilisation conditions on the rheological properties of thermoresponsive pluronic F-127-based gels for the ophthalmic use', *Acta Pol. Pharm. Drug Res.*, vol. 75, no. 2, pp. 471–481, June 2018, doi: 10.32383/appdr/146102.
- [96] M. C. Beard *et al.*, 'Autoclaving of Poloxamer 407 hydrogel and its use as a drug delivery vehicle', *J. Biomed. Mater. Res. B Appl. Biomater.*, vol. 109, no. 3, pp. 338–347, Mar. 2021, doi: 10.1002/jbm.b.34703.
- [97] I. Ferreira, A. C. Marques, P. C. Costa, and M. H. Amaral, 'Effects of Steam Sterilization on the Properties of Stimuli-Responsive Polymer-Based Hydrogels', *Gels*, vol. 9, no. 5, p. 385, May 2023, doi: 10.3390/gels9050385.
- [98] J. M. White and M. A. Calabrese, 'Impact of small molecule and reverse poloxamer addition on the micellization and gelation mechanisms of poloxamer hydrogels', *Colloids Surf. Physicochem. Eng. Asp.*, vol. 638, p. 128246, Apr. 2022, doi: 10.1016/j.colsurfa.2021.128246.

- [99] G. Russo *et al.*, 'Tuning Pluronic F127 phase transitions by adding physiological amounts of salts: A rheology, SAXS, and NMR investigation', *Eur. Polym. J.*, vol. 204, p. 112714, Jan. 2024, doi: 10.1016/j.eurpolymj.2023.112714.
- [100] S. Kamlungmak *et al.*, 'Lamellar phase behavior and molecular interaction of a thermoresponsive poloxamer and crosslinked poly (vinyl alcohol) hydrogel', *Mater. Today Commun.*, vol. 20, p. 100542, Sept. 2019, doi: 10.1016/j.mtcomm.2019.100542.
- [101] A.-S. Huysecom *et al.*, 'Phase behavior of medium-length hydrophobically associating PEO-PPO multiblock copolymers in aqueous media', *J. Colloid Interface Sci.*, vol. 641, pp. 521–538, July 2023, doi: 10.1016/j.jcis.2023.03.013.
- [102] K. A. Gaidhani, M. Harwalkar, D. Bhambere, and P. S. Nirgude, 'LYOPHILIZATION / FREEZE DRYING A REVIEW'.
- [103] K. R. Miller, C. S. Prescott, T. L. Jacobs, and N. L. Lassignal, 'Artifacts associated with quick-freezing and freeze-drying', *J. Ultrastruct. Res.*, vol. 82, no. 2, pp. 123–133, Feb. 1983, doi: 10.1016/S0022-5320(83)90047-3.
- [104] A. Vásquez-Rivera *et al.*, 'Use of sucrose to diminish pore formation in freezedried heart valves', Sci. Rep., vol. 8, no. 1, p. 12982, Aug. 2018, doi: 10.1038/s41598-018-31388-4.
- [105] J. Aigoin *et al.*, 'Comparative Analysis of Electron Microscopy Techniques for Hydrogel Microarchitecture Characterization: SEM, Cryo-SEM, ESEM, and TEM', ACS Omega, vol. 10, no. 15, pp. 14687–14698, Apr. 2025, doi: 10.1021/acsomega.4c08096.
- [106] A. M. Heimbuck, T. R. Priddy-Arrington, B. J. Sawyer, and M. E. Caldorera-Moore, 'Effects of post-processing methods on chitosan-genipin hydrogel properties', *Mater. Sci. Eng. C*, vol. 98, pp. 612–618, May 2019, doi: 10.1016/j.msec.2018.12.119.
- [107] A. Arsiccio and R. Pisano, 'The Preservation of Lyophilized Human Growth Hormone Activity: how Do Buffers and Sugars Interact?', *Pharm. Res.*, vol. 35, no. 7, p. 131, Apr. 2018, doi: 10.1007/s11095-018-2410-9.
- [108] C. Berrouet, N. Dorilas, K. A. Rejniak, and N. Tuncer, 'Comparison of Drug Inhibitory Effects (\$\$\hbox {IC}_{50}\$\$) in Monolayer and Spheroid Cultures', *Bull. Math. Biol.*, vol. 82, no. 6, p. 68, June 2020, doi: 10.1007/s11538-020-00746-7.
- [109] O. Kadioglu *et al.*, 'Identification of metastasis-related genes by genomic and transcriptomic studies in murine melanoma', *Life Sci.*, vol. 267, p. 118922, Feb. 2021, doi: 10.1016/j.lfs.2020.118922.
- [110] J. Nakayama *et al.*, 'Differential Cell- and Immuno-Biological Properties of Murine B16-F1 and F10 Melanomas: Oncogene c-fos Expression, Sensitivity to LAK Cells and/or IL-

- 2, and Components of Gangliosides', *J. Dermatol.*, vol. 22, no. 8, pp. 549–559, 1995, doi: 10.1111/j.1346-8138.1995.tb03873.x.
- [111] Y. Salama, S.-Y. Lin, D. Dhahri, K. Hattori, and B. Heissig, 'The fibrinolytic factor tPA drives LRP1-mediated melanoma growth and metastasis', *FASEB J.*, vol. 33, no. 3, pp. 3465–3480, 2019, doi: 10.1096/fj.201801339RRR.
- [112] P. Lopez-Bergami, 'The role of mitogen- and stress-activated protein kinase pathways in melanoma', *Pigment Cell Melanoma Res.*, vol. 24, no. 5, pp. 902–921, 2011, doi: 10.1111/j.1755-148X.2011.00908.x.
- [113] S. D. Scilabra *et al.*, 'Increased TIMP-3 expression alters the cellular secretome through dual inhibition of the metalloprotease ADAM10 and ligand-binding of the LRP-1 receptor', *Sci. Rep.*, vol. 8, no. 1, p. 14697, Oct. 2018, doi: 10.1038/s41598-018-32910-4.
- [114] S. D. Scilabra *et al.*, 'Dissecting the interaction between tissue inhibitor of metalloproteinases-3 (TIMP-3) and low density lipoprotein receptor-related protein-1 (LRP-1): Development of a "TRAP" to increase levels of TIMP-3 in the tissue', *Matrix Biol.*, vol. 59, pp. 69–79, May 2017, doi: 10.1016/j.matbio.2016.07.004.
- [115] 'Vitamin E TPGS-Poloxamer Nanoparticles Entrapping a Novel PI3Kα Inhibitor Potentiate Its Activity against Breast Cancer Cell Lines'. Accessed: Oct. 08, 2025. [Online]. Available: https://www.mdpi.com/1999-4923/14/9/1977
- [116] G. Dumortier, J. L. Grossiord, F. Agnely, and J. C. Chaumeil, 'A Review of Poloxamer 407 Pharmaceutical and Pharmacological Characteristics', *Pharm. Res.*, vol. 23, no. 12, pp. 2709–2728, Dec. 2006, doi: 10.1007/s11095-006-9104-4.
- [117] R. I. El-Gogary, S. A. A. Gaber, and M. Nasr, 'Polymeric nanocapsular baicalin: Chemometric optimization, physicochemical characterization and mechanistic anticancer approaches on breast cancer cell lines', *Sci. Rep.*, vol. 9, no. 1, p. 11064, July 2019, doi: 10.1038/s41598-019-47586-7.
- [118] R. Minnes, M. Nissinmann, Y. Maizels, G. Gerlitz, A. Katzir, and Y. Raichlin, 'Using Attenuated Total Reflection–Fourier Transform Infra–Red (ATR–FTIR) spectroscopy to distinguish between melanoma cells with a different metastatic potential', *Sci. Rep.*, vol. 7, no. 1, p. 4381, June 2017, doi: 10.1038/s41598–017-04678–6.
- [119] M. Tuszynska, J. Skopinska-Wisniewska, M. Bartniak, and A. Bajek, 'Conceptualization and Preliminary Characterization of Poloxamer-Based Hydrogels for Biomedical Applications', *Bioconjug. Chem.*, vol. 36, no. 6, pp. 1169–1179, June 2025, doi: 10.1021/acs.bioconjchem.5c00030.